
TESSERA: Temporal Embeddings of Surface Spectra for Earth Representation and Analysis

Zhengpeng Feng¹, Clement Atzberger^{2†}, Sadiq Jaffer^{1†}, Jovana Knezevic³,
 Silja Sormunen⁴, Robin Young¹, Madeline C Lisaius¹, Markus Immitzer²,
 David A. Coomes³, Anil Madhavapeddy¹, Andrew Blake⁵, Srinivasan Keshav^{1*}

¹ Department of Computer Science and Technology, University of Cambridge, UK

² dClimate Labs, New York, USA ³ Department of Plant Sciences, University of Cambridge, UK

⁴ Department of Computer Science, Aalto University, Finland

⁵ Clare Hall, University of Cambridge, UK

† Equal contribution. *Corresponding author. Email: sk818@cam.ac.uk.

Abstract

Satellite remote sensing from repeated observations and multiple sensors enables a wide range of downstream applications, including climate modeling, carbon accounting, and strategies for conservation and sustainable land use. However, satellite time series are voluminous, often corrupted by sensor noise, clouds, and atmospheric conditions, and unevenly spaced in time, making them challenging to use. We present TESSERA, an open, global, land-oriented remote sensing foundation model that uses self-supervised learning to generate ‘ready-to-use’ embeddings at 10 m scale from pixel-level satellite time series data. TESSERA uses two parallel Transformer-based encoders to combine optical data from ten Sentinel-2 spectral bands at 10-60 m spatial resolution and two Sentinel-1 synthetic aperture radar backscatter coefficients at 10 m resolution to create embeddings that are subsequently fused with a multilayer perceptron to create annual global embedding maps. We compare our work with state-of-the-art task-specific models and other foundation models in five diverse downstream tasks and find that TESSERA closely matches or outperforms these baselines. We believe that TESSERA’s ease of use, openness, computation-, label-, and data-efficiency, and high performance will prove transformative in a wide range of ecological applications.

Monitoring Earth’s dynamic systems through satellite Earth Observation (EO) is critical to addressing global challenges including food security, forest and biodiversity loss, climate change, and disaster mitigation [118, 183, 24]. Petabytes of EO data are available from sensors in various modalities, and declining launch costs promise exponential growth in the future [176]. However, practitioners face a fundamental bottleneck: the scarcity of large, accurately labeled datasets required for supervised training [95]. The direct use of EO data also presents challenges as data quality is affected by sensor noise, cloud cover, atmospheric effects, and nonuniform temporal sampling, preventing full and easy use of this valuable resource [193, 60, 130].

EO data users usually mitigate these issues by annual or seasonal compositing [34], then using supervised machine learning to map from composited images to task-specific classification, such as crop identification [8]. However, compositing removes the critical temporal signal arising from phenology and training a task-specific ML model is computationally onerous. Recent EO approaches tackle the latter problem using *foundation models*: general-purpose models pre-trained on a broad set of EO data [178]. Their development follows several paths, including

supervised pre-training on large labeled datasets for spatio-temporal analysis [21, 20, 160, 18], and various self-supervised learning (SSL) strategies that learn from the inherent structure of the data itself. These SSL techniques include generative methods, such as masked autoencoders [32, 104, 126, 61, 113, 94, 112, 53, 144, 140, 134, 67, 149], diffusion-based models [192, 80, 115], and contrastive methods that learn efficient representations by comparing data samples [14, 102, 7, 99, 81, 23, 59, 70, 169]. Subsequently, these general purpose models are adapted and fine-tuned for specific remote sensing tasks such as high-resolution (semantic) segmentation [161, 177, 184, 28, 191].

Although existing SSL approaches create rich multidimensional ‘embeddings’ from unlabeled data through auxiliary tasks that reveal latent patterns [15, 97], they still do not address the loss of the temporal signal during compositing. In recent work, Lisaius et al [95] have demonstrated that the Barlow Twins loss [187], grounded in redundancy reduction principles [17], can be adapted to preserve the spectral-temporal signal in latent embeddings when processing dense EO time series. Building on this insight, we introduce TESSERA, a pixel-oriented foundation model for EO time series that creates 128-dimensional latent embeddings at 10m resolution and global scale to enable state-of-the-art performance across a diverse array of complex tasks. Our experiments demonstrate that these TESSERA-derived embeddings outperform baseline methods in tasks as diverse as estimating canopy height in rainforests in Borneo, detecting crop types in Austria, and identifying fire scars in California.

Importantly, our outputs are ‘ready to use’: Users need neither to fine-tune the model, nor download and process voluminous satellite data, nor perform inferencing other than what is needed to perform a downstream task. This makes TESSERA frugal in terms of both data handline and computation. They can also keep their data private instead of having to upload it to a centralized repository. This removes a crucial barrier to use. We demonstrate that TESSERA is label-efficient: Only a relatively small number of labels for task-specific training are needed to achieve state-of-the-art performance. Moreover, our model is open source, enabling extensibility and scientific reproducibility.

We have made a gap-free, global, annual, 10-meter resolution embedding map for 2024 openly available through the GEOTESSERA Python library [152] and aim to eventually provide global maps for the entire period 2017-2024. These information-rich precomputed maps greatly simplify a wide range of downstream EO applications. We have also released interactive and batch tools for habitat mapping using TESSERA embeddings (see [1] for details).

To our knowledge, TESSERA is unprecedented in its ease of use, scale, and accuracy: no other foundation model provides analysis-ready outputs, is open, and provides global, annual coverage at 10m resolution using only spectral-temporal features at pixel level (Supplementary Text: 5).

1 Overview of the TESSERA System

TESSERA uses self-supervised learning to create per-pixel embeddings from the unlabeled time-series of observations from Sentinel-1 (SAR) and Sentinel-2 Multispectral Instruments (MSI), learning complementary information from the optical and microwave data streams. It comprises two main components: a dual-branch encoder and a projector network (see Fig. 1 for details).

TESSERA models its input as a set of ‘d-pixels.’ Each d-pixel represents the annual time series of Sentinel-1 and Sentinel-2 observations at a specific 10 m pixel on Earth as a two-dimensional array ordered in time (that is, channels \times timesteps). This format preserves the temporal evolution of spectral/backscatter signatures inherent in the satellite data. Our design accommodates common observational gaps and irregularities, such as those due to cloud cover or orbit overlap, by masking invalid rows, which are handled during subsequent processing stages. Model training and inferencing is done by sparse temporal sampling followed by flattening of these d-pixels (see Appendix A.4 and Fig. 1 for details). For each 10 m pixel, the fused TESSERA encoders generate a compact (8 bit), 128-dimensional embedding that encapsulates that pixel’s annual temporal and spectral characteristics. Under typical mid-latitude observation conditions, this compresses input data by a factor of ≈ 24 , with higher compression ratios at higher latitudes.

TESSERA uses two separate, parallel Transformer-based encoders: one for Sentinel-1 SAR backscatter data in the C-band (VV and VH polarizations) and another for Sentinel-2 MSI data (10 spectral bands covering the visible, near, and shortwave infrared). Each encoder processes the

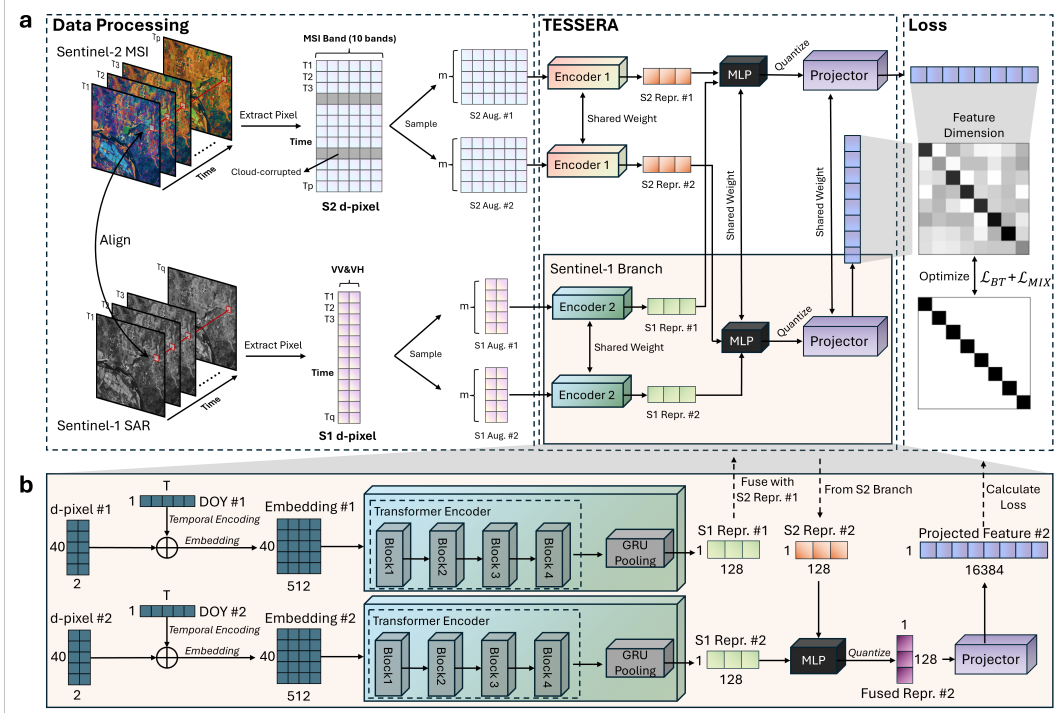


Figure 1: **Architecture and data processing pipeline of the TESSERA foundation model.** **a**, Overview of the end-to-end workflow. Spatially aligned time-series data from Sentinel-2 MSI and Sentinel-1 SAR are first extracted for each pixel location, forming modality-specific ‘d-pixels’. For self-supervised training, two distinct augmentations are created from each d-pixel—each augmentation is a random cloud-free sample from an annual time series of Sentinel-2 observations along with the corresponding Sentinel-1 data—processed through a dual-branch architecture with *weights shared between the branches*. The resulting 128-dimensional embeddings from both modalities are fused by a multilayer perceptron (MLP) to create the output embeddings of the system. The fused features are then expanded to 16,384 dimensions by a large projector network. A modified Barlow Twins loss ($\mathcal{L}_{BT} + \mathcal{L}_{MIX}$) is calculated on the cross-correlation matrix of these projected features, optimizing the model to learn augmentation-invariant and decorrelated embeddings that are internally decorrelated, and fairly invariant to obscured days in the Sentinel-2 time series. **b**, Detailed structure of a single encoder branch. A d-pixel, represented as a matrix of temporal steps versus spectral bands (40 time-steps \times 2 bands for Sentinel-1), is first embedded. A Day-of-Year-based temporal encoding is added to these embeddings. The resulting sequence is then processed by an 4-block Transformer Encoder. Finally, a Gated Recurrent Unit (GRU) pooling layer processes the sequence of temporal features; its final hidden state, which summarizes the entire time series, serves as the single 128-dimensional embedding for that modality, which is then passed to the fusion MLP shown in panel **a**.

temporal sequence of a d-pixel, utilizing multi-head self-attention mechanisms to capture complex temporal dependencies and patterns specific to each data modality. Positional encodings derived from the Day-of-Year (DoY) are incorporated to provide temporal context. An attention pooling layer within each encoder aggregates the temporal features into a fixed-size vector that represents the annual signature for that modality [1]. See Appendix A.7 and Figure 1 for architectural details.

Modality-specific embeddings derived from dual encoders are first fused using a multilayer perceptron (MLP) which is trained alongside the encoders. This fused embedding, which serves as the 128-dimensional pixel embedding for downstream tasks, is then quantized before being fed into a high-dimensional projector network. This projector, a significantly larger MLP, expands the dimensionality of the fused representation to facilitate effective redundancy reduction during the self-supervised learning phase. A detailed breakdown of the model’s architectural parameters is provided in Appendix A.6 (Table 2).

1.1 Model Training

TESSERA learns the mapping of inputs to embeddings through a self-supervised pretraining process on a large-scale, unlabeled global dataset. It is trained by optimizing a modified Barlow Twins loss function [187, 95]. The core principle is to learn embeddings that are invariant to differing views of the same pixel’s optical-band data (e.g., different subsets of cloud-free observation dates) while minimizing redundancy between the learned feature dimensions. This is achieved by generating two distinct augmented views for each input d-pixel, through independent sparse temporal samples. This avoids creating augmentations by applying artificial (e.g. hand-crafted) distortions. The model then learns to reconcile these partial views. The loss function includes the standard Barlow Twins terms for invariance and redundancy reduction, complemented with an additional mix-up regularization term to enhance robustness and intersample interaction during training (see Appendix A.7.2 for the full loss function, Equation 11). In practice, we randomly sub-sample each d-pixel three times, to create a total of three pairs of augmentations.

The pretraining phase utilizes a vast global dataset comprising approximately 800 million d-pixels, down-sampled from Sentinel-1 and Sentinel-2 imagery (we use a downsampling ratio of 400:1). To ensure successful generalization, a multilevel data sampling, shuffling, and batching strategy was developed. This ensured that each training mini-batch contained a highly diverse set of d-pixels from various geographic locations and acquisition conditions, preventing model overfitting and promoting the learning of universally applicable features. The model was trained for one epoch on this dataset using distributed training techniques (see Appendix A.7.3 for further details on data preparation, the shuffling strategy and optimization). The key hyperparameters used during pretraining are summarized in Appendix A.7.3 (Table 3).

1.2 Model Inference and Global Embeddings Maps

Following pretraining, the TESSERA dual encoder (with frozen weights and excluding the projector) is used to generate an annual 128-dimensional embedding for every 10-meter pixel globally. This involves making inferences from a sample of length 40 from the annual Sentinel-1 and Sentinel-2 time series for each pixel through the trained encoders. To ensure that our maps are gap-free, random sampling with replacement is used to generate augmentations from d-pixels that have fewer than 40 non-cloudy observations. The primary output of this inference stage is a set of annual, global, 10-meter resolution TESSERA embedding maps. These maps are designed as readily usable multichannel geospatial data layers. This “Embeddings-as-Data” approach significantly lowers the barrier to entry for end-users, as these rich, precomputed features can be directly ingested by downstream models without the need for raw satellite data processing or running the TESSERA model itself (see Appendix A.8). We are generating global embeddings for 2024 (approx. 250 TB) and will progressively extend coverage backward year by year until 2017.

2 Downstream Tasks

The effectiveness and generalizability of the TESSERA embeddings are evaluated on a diverse range of downstream remote sensing tasks. These include, but are not limited to, pixel-wise classification (e.g., crop type mapping), pixel-wise regression (e.g., canopy height and AGB estimation) and patch-based dense predictions (for example, semantic segmentation). In these evaluations, the pre-trained TESSERA encoder acts as a fixed feature extractor; given adequate computing resources, fine-tuning of the model is also possible. Lightweight, task-specific model heads (e.g., shallow MLPs or UNet-style decoders) are then trained using these fixed embeddings. This approach typically requires substantially less labelled data and computational resources compared to training deep models from scratch, yet achieves or surpasses the state of the art. See Appendix D and Supplementary Fig. 10 for the general downstream application workflow.

We have studied how the model’s performance on a typical downstream task improves as we increase the projector dimension (responsible for more than 95% of the model’s parameters) and the amount of computing as well as carried out an ablation study to understand which model components and design decisions are mainly responsible for performance [1].

2.1 Crop Type Classification

Agricultural monitoring through EO is a cornerstone of managing global food security, providing critical data to stakeholders in the agricultural sector [175]. The classification of crop types informs vital agricultural decisions by allowing accurate estimates of crop area and production, and facilitating low-cost monitoring of diseases and pests in vast regions [60]. However, this task is considerably more complex than many other challenges in the classification of land cover, as it requires discerning subtle spectral and temporal variations that differentiate different crop classes [60]. In the past, classifiers such as Random Forest (RF) applied to hand-crafted composite time series data have established the standard [60, 114]. Recent advances have shifted towards foundation models, which, unlike bespoke machine learning models that require region-specific feature extraction and training, offer generalizable representations that can be applied universally [6, 79]. Here, we demonstrate that TESSERA’s precomputed embeddings set a new state-of-the-art.

To evaluate performance, we used the INVEKOS Austrian crop dataset [3] from the 2021–2022 growing season. This is an extensive data set that covers 1850 km² east of Vienna with 154 different crop types, which we consolidated into 17 classes based on crop similarity (e.g., merging feed beet with sugar beets) [3]. We compared the performance of a lightweight classification head trained on TESSERA embeddings against three key baselines: (1) an RF classifier trained on engineered temporal features from raw satellite data, (2) the PRESTO foundation model [149], and (3) Google Satellite Embedding (GSE) [56]. For the foundation models, we applied the same lightweight head to their respective embeddings for a direct comparison. We evaluated performance using multiple metrics, including F1 scores, under varying data availability scenarios, from 30% of labelled data to one-shot learning. We also evaluated performance on a patch-based semantic segmentation task against several other foundation models. Details on data processing, model architectures, and training protocols are provided in Appendix E.

TESSERA consistently surpasses both baselines in all training regimes, especially in settings where labeled data are scarce (Fig. 2). In pixel-wise classification tasks with training data splits from 1% to 30%, a simple MLP trained on TESSERA embeddings achieves higher weighted and macro F1 scores than an identical MLP trained on PRESTO or GSE embeddings, and substantially outperforms the RF baseline (Fig. 2a). TESSERA also maintains statistically significant advantages in one-shot and few-shot scenarios (Fig. 2b). Furthermore, TESSERA’s utility extends to patch-based semantic segmentation, where it consistently achieves higher mIoU and macro F1 scores compared to other leading foundation models, including PRESTO and GSE, across various patch sizes (Fig. 2c).

These performance gains are due to the high quality of the learned embeddings. A UMAP analysis [103] of the embedding space reveals that TESSERA embeddings form tighter, more semantically coherent clusters by crop class compared to those from both PRESTO and GSE (Fig. 2d). This improved separability highlights the strength of TESSERA as a foundational tool for agricultural applications.

2.2 Canopy height estimation

Canopy height is a key structural attribute of forests, linked to above-ground biomass and carbon stocks, and therefore important for climate mitigation efforts and carbon accounting frameworks such as REDD+ [106, 49]. It is correlated with ecosystem function [105], forest age, and successional stage, while also serving as a proxy for habitat quality, an important determinant of biodiversity patterns and species richness [37, 25, 136]. Accurate, scalable canopy height models (CHMs) can enable detection of forest degradation and disturbance.

Despite substantial progress in global canopy height mapping, current approaches exhibit limitations that restrict their reliability and applicability. GEDI, a spaceborne LiDAR system, can provide reasonably accurate canopy height measurements to train models to generate CHMs from optical and radar data; however, it does not provide wall-to-wall maps, and does not sample high latitudes [41], and produces unreliable estimates in mountainous terrain [52]. Radar-based CHMs (e.g., TanDEM-X) achieve global coverage, but are affected by canopy height saturation in dense forests and depend on high-quality terrain models to accurately isolate canopy height [131]. Optical data, while widely available, lack inherent sensitivity to vertical structure and require indirect proxies or fusion with information from active sensors [158, 96] - yet none of the three most widely used global CHM

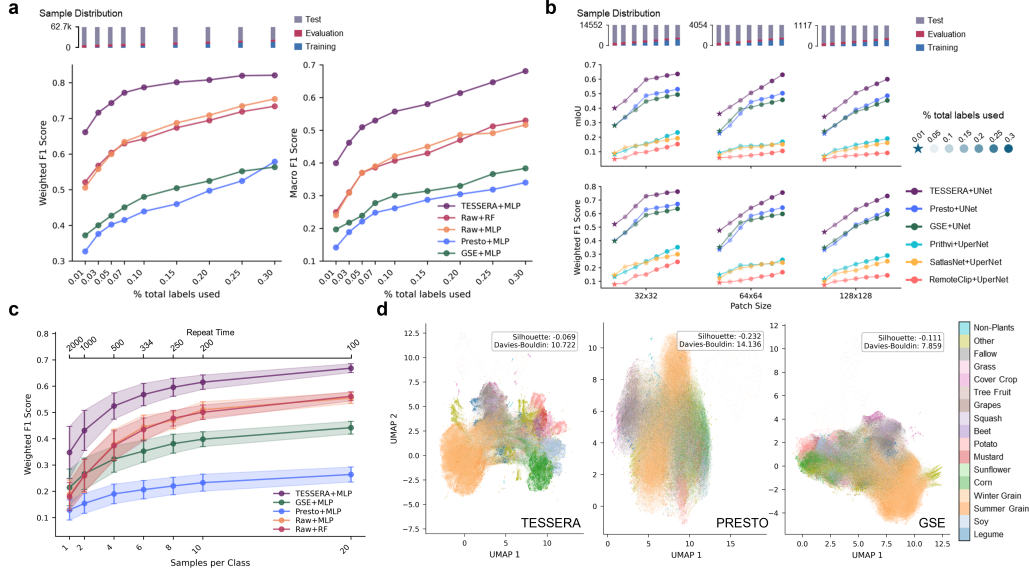


Figure 2: TESSERA embeddings achieve state-of-the-art performance in crop type classification. The evaluation was conducted on the 2022 Austrian crop dataset. **a**, Weighted and Macro F1 scores for pixel-wise classification as a function of the training data ratio. TESSERA embeddings, coupled with a simple MLP, consistently outperform a Random Forest model and other foundation models like PRESTO and Google Satellite Embedding (GSE). **b**, Patch-based semantic segmentation performance comparison. TESSERA embeddings, used with a UNet model, achieve higher mean Intersection over Union (mIoU) and Macro F1 scores than other foundation models across various patch sizes and training data ratios. **c**, Weighted F1 score in few-shot learning scenarios. TESSERA maintains a significant performance advantage even with very few training samples per class. Error bars represent the standard deviation over multiple runs. **d**, UMAP visualization of the embedding spaces for TESSERA, PRESTO, and GSE for 17 crop classes. TESSERA’s embeddings exhibit clearer separation and more coherent clustering visually.

models currently implement sensor fusion [84, 121, 148]. Most approaches instead rely on a single sensor type and derive height predictions either from temporal composites or from large numbers of hand-engineered features (e.g., > 500 features in Potapov et al. [121]), which may generalize poorly across ecosystems. These models tend to underestimate tall canopies, especially in tropical forests where most of the above-ground carbon is stored, and face challenges from persistent cloud cover, sensor saturation [83], and inconsistencies in input quality. As a result, significant discrepancies remain between global CHMs and airborne LiDAR benchmarks, and current products underestimate local variability and structural extremes [107]. Most CHMs are also static, failing to capture inter-annual dynamics, and inconsistencies in methodology and sensor characteristics hinder cross-product integration. These limitations underscore the need for scalable, temporally resolved, and sensor-fused CHMs with quantified uncertainties to support forest monitoring, carbon accounting, and Earth system modelling [108, 116].

We evaluated TESSERA embeddings to predict canopy height at 10 m resolution within a 5×6 km area of tall old-growth tropical forests in the Danum Valley, Borneo [74] with openly available ground-truth data [33]. To ensure spatial independence, we conducted four-fold spatial cross-validation against the airborne LiDAR-derived canopy height, each time holding out a contiguous 50% of the region for testing and using the remaining 50% for training and validation. A 30-million-parameter UNet was trained using 32×32 pixel patches of the embeddings as input. To account for variability in training convergence, we performed three independent training runs per fold, each for 200 epochs, and retained the model with the best performance on the validation set. The accuracy metrics for the foundation models are reported as the average across the 12 runs. TESSERA achieved an R^2 of 0.66, a root mean squared error (RMSE) of 8.88 m, and a mean bias of -0.62 m.

We benchmarked TESSERA’s performance against state-of-the-art approaches through three sets of comparisons (Fig. 3). First, we evaluated its predictions against three global canopy height products: the GLAD map by Potapov et al. [121], the ETH map by Lang et al. [84], and the Meta map

by Tolan et al. [148]. Although local models generally outperform global products in regional evaluations [127], the pronounced saturation of these global models at much lower canopy heights - combined with RMSEs that exceed their reported global averages [121, 84, 148]—underscores the challenge of accurately mapping structurally complex high canopy regions such as Danum Valley.

We also compared our results to regional wall-to-wall canopy height maps for Indonesia, Malaysia, and the Philippines produced by Lang et al. [85], which used deep convolutional neural networks trained on Sentinel-2 time series and GEDI LiDAR to estimate regional canopy height and biomass. Second, we compared TESSERA to two alternative pixel-based foundation models, PRESTO [149] and Google Satellite Embedding (GSE) [56], using the same U-Net architecture, but replacing TESSERA’s input representations with those of the other foundation models. Finally, to assess the added value of the learned representations over the raw input data, we trained the same U-Net using cloud-free annual median composites of Sentinel-2 imagery.

In all comparisons, TESSERA outperformed competing methods. Moreover, its embeddings do not require pre-processing, greatly enhancing reproducibility. Instead, only the region and year of interest are needed to replicate the input data pipeline. By fusing Sentinel-1 and Sentinel-2 data without requiring preprocessing or feature engineering, TESSERA’s 128-dimensional embeddings encode cloud-free, information-rich signals that effectively address key challenges in canopy height modelling.

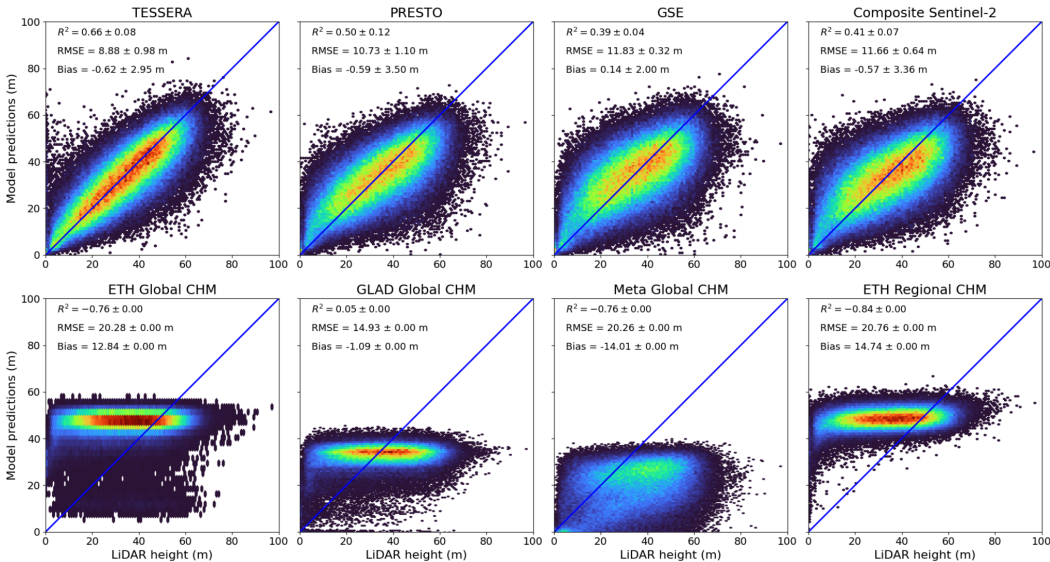


Figure 3: **TESSERA outperforms global and regional models as well as alternative pixel-based foundation models in canopy height estimation.** Predicted canopy height (y-axis) is compared against airborne LiDAR reference data (x-axis) across multiple models and input datasets in Danum Valley, Borneo. **Top row:** Predictions from models trained using different input representations—TESSERA, PRESTO, Google Satellite Embedding (GSE), and raw Sentinel-2 composites—using the same model architecture and training procedure. TESSERA achieves the highest coefficient of determination and the lowest RMSE (8.88 ± 0.98 m), indicating superior performance in structurally complex, tall tropical canopies. **Bottom row:** Comparisons to existing global and regional canopy height maps, including products from ETH, GLAD, Meta, and Lang et al.’s regional CHM. All four products show substantially lower predictive performance ($R^2 < 0.05$, $RMSE > 14$ m), with three exhibiting negative correlations. These models saturate at lower canopy heights and show large bias and RMSE, highlighting the limitations of global products when applied to high-biomass tropical forests without local calibration. A 1:1 reference line (blue) is shown in each panel for comparison.

2.3 Above-ground biomass estimation

Forests play a central role in the global carbon cycle, creating a pressing need for reliable and scalable AGB estimates for climate modeling, carbon accounting, and informed strategies for conservation and sustainable land use [66]. Accurate estimation of above-ground biomass (AGB) is essential to quantify forest carbon stocks and monitor temporal changes due to deforestation, degradation, and recovery [45].

We evaluated the performance of TESSERA in predicting AGB against two leading models on a benchmark dataset. Firstly, we considered the geospatial foundation model SpectralGPT [67] combined with a UPerNet regression head – a setup found in the Pangaea benchmark [101] to outperform other foundation models tested on the BioMassters dataset [111]. As the preprocessing pipeline is not yet available in the codebase of Ref. [67] at the time of our analysis, we adopted the implementation from Ref. [101], which uses the preprocessed satellite imagery from the BioMassters dataset as input. Secondly, we used the winning model from the BioMassters competition as our state-of-the-art supervised baseline – a UNet with a temporal attention encoder [111], which achieved the lowest RMSE among over 1,000 submissions. The BioMassters dataset comprises 11,462 image patches that represent above-ground biomass in Finnish forests from 2017 to 2021. Ground-truth AGB values are derived from airborne LiDAR and aerial imagery, using calibrated allometric equations informed by extensive field plots by the Finnish Forest Centre and National Land Survey. Each patch covers a $2560 \times 2560 \text{ m}^2$ area, with a spatial resolution of 10 m per pixel. The fine spatial granularity of the dataset makes the estimation task more challenging, as it introduces a long, thin tail of high AGB values that would not appear in coarser-resolution data.

A comparison of RMSE across varying training label fractions (Fig. 4a) shows that a UNet trained on the TESSERA embeddings consistently surpasses a UPerNet trained on the SpectralGPT representations, achieving lower prediction errors on 1% of the training set than SpectralGPT on the full training set. These results underscore the robustness of TESSERA in sparse-label regime. Moreover, TESSERA achieves results comparable to those of the supervised baseline trained on the full dataset, even with limited label availability. In general, bespoke models are inherently difficult to surpass in fully supervised settings. It is worth noting that the comparison to benchmarks is not entirely straightforward, as the satellite data used in the benchmark models differs from the TESSERA input. However, these discrepancies can be considered as an inherent part of the respective processing pipelines and hence largely unavoidable.

2.4 Burned Area Detection

The frequency and severity of wildfires are projected to increase in many parts of the world due to climate change [5, 71, 117]. Accurate maps of burned areas and burn severity are critical for monitoring wildfire trends [10], predicting wildfire occurrence [29], assessing ecosystem recovery [186], and establishing effective fire management strategies [63]. Remote sensing is widely used to detect burned areas and assess severity regionally and globally [82].

Most existing burn area mapping approaches rely on time series analysis or direct comparison between pre-fire and post-fire images, often requiring careful selection of suitable cloud-free images, manually tuned thresholds, and expert input [82, 119]. These methods typically use spectral indices such as the Normalized Burn Ratio (NBR), though many studies have also explored the design of custom features and applied spectral dimensionality reduction techniques to preserve key fire-related signals [82]. Most existing methods use optical sensors [82], which can detect fire-specific spectral signatures but are susceptible to cloud cover [64], particularly problematic for fire detection in ecosystems where vegetation rapidly re-greens [65]. SAR offers complementary sensitivity to vegetation structure and is unaffected by cloud cover [82, 143, 154]. Recent reviews emphasize the need for sensor fusion, combining passive and active sensors to improve accuracy and robustness [82, 30]. Sentinel-1 and 2 sensors in particular, when combined together at 10 m resolution, have shown promise in detecting burn areas from small fires that are often left out of coarse, global burn area products [143, 154, 129]. TESSERA extends the philosophy of traditional approaches by encoding temporal dynamics, while addressing major limitations through sensor fusion and the use of data-driven features learned directly from large volumes of combined Sentinel-1 and Sentinel-2 imagery (Fig. 5).

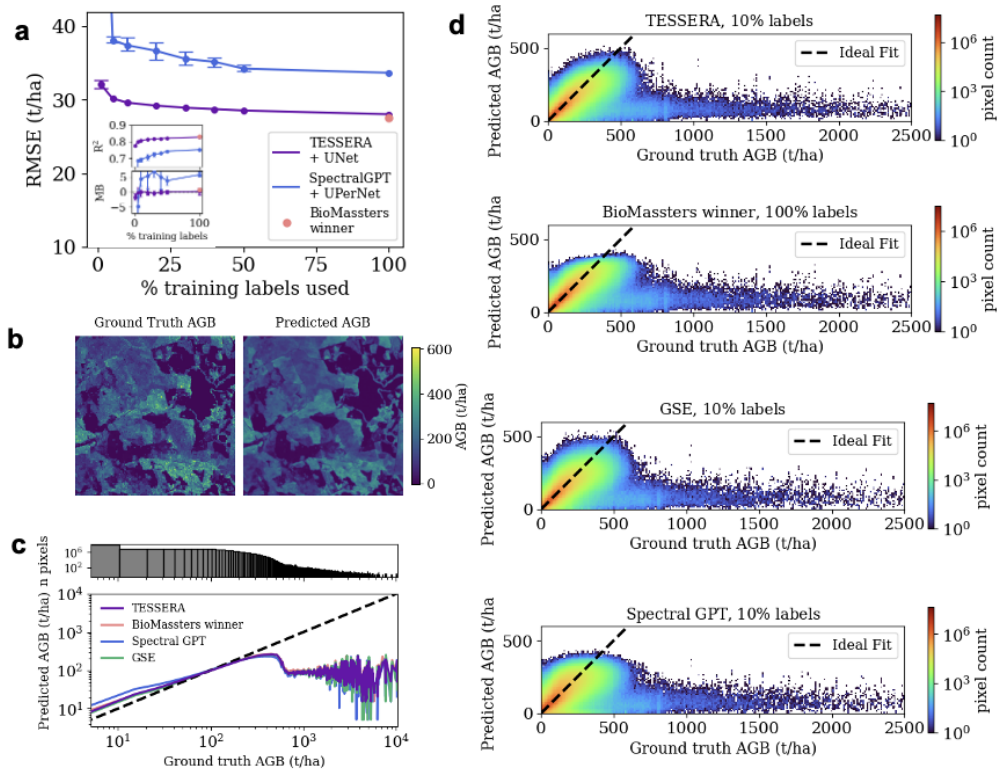


Figure 4: TESSERA embeddings demonstrate robustness for AGB mapping under limited label availability. **a**, TESSERA achieves lower RMSE values than the foundation model benchmark SpectralGPT. Following the evaluation protocol in Ref. [111], RMSE is computed on a fixed test set of 2773 patches and reported as the average RMSE per patch. For limited labels testing, a subset of labels is randomly chosen from the remaining data, and randomly split into training and validation sets (80:20). The figure shows the average RMSE computed over five random splits, with bars indicating the minimum–maximum range when it exceeds the size of the dot. The UNet model is trained on the TESSERA embeddings for 80 epochs, with the model achieving the lowest loss on the validation set selected as the final model. The inset depicts the coefficient of determination (R^2) and mean bias (MB) as functions of label availability. **b**, Predicted AGB map for an example patch using 10% of the training labels. **c**, The mean predicted AGB values show increasing bias at higher ground-truth AGB values, which are sparse in the dataset. The top panel depicts the histogram of the ground-truth AGB values. **d**, Pixel-wise comparison of predicted versus ground-truth AGB values for the test data with TESSERA+UNet (top), the supervised baseline (middle) and SpectralGPT+UPerNet (bottom).

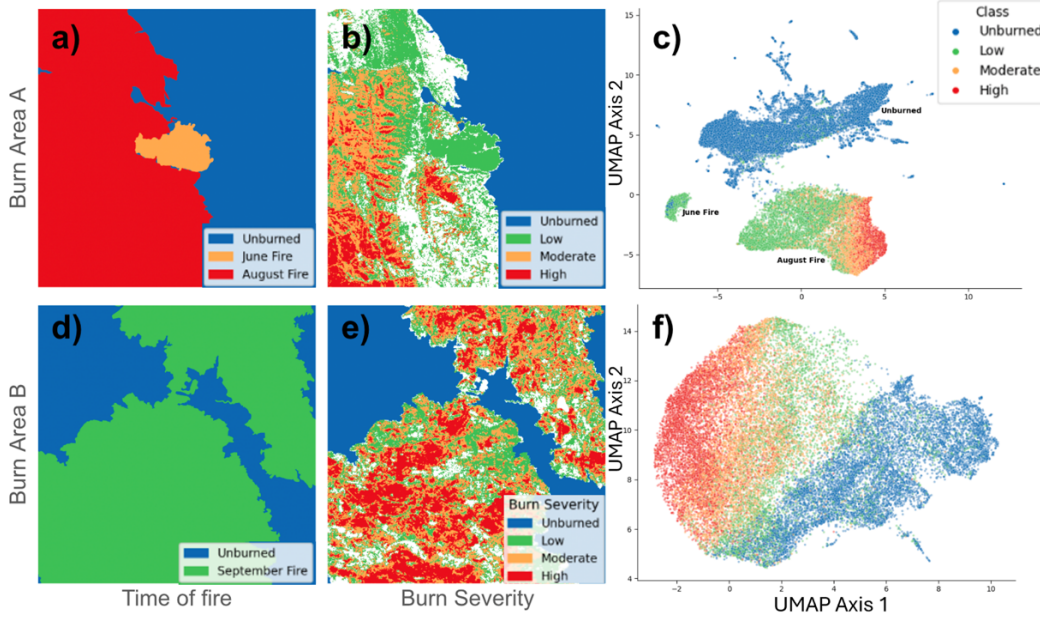


Figure 5: **TESSERA embeddings capture wildfire extent, timing, and severity across two burned regions.** (a–c) Burn Area A, which experienced two distinct fires in June and August 2021. (a) Time of fire map based on MTBS, showing unburned areas (blue), the June fire (orange), and the August fire (red). (b) Burn severity classification for the same region, with unburned (blue), low (green), moderate (orange), and high (red) severity. (c) UMAP projection of TESSERA embeddings from 2021, with colors corresponding to burn severity. Embeddings form well-separated clusters for unburned, June-, and August-burned areas, with a visible internal gradient reflecting severity within August fire. (d–f) Burn Area B, which experienced a single large fire in September 2021. (d) Time of fire map showing unburned (blue) and burned (green) areas. (e) Burn severity classification showing heterogeneous severity across the landscape. (f) UMAP projection for Burn Area B, revealing fuzzier boundaries between burned and unburned pixels, though the severity gradient remains evident.

We tested whether TESSERA’s temporal embeddings capture fire-induced changes in spectral and radar signals. We evaluated its ability to detect burned areas and burn severity using two randomly selected 15×15 km regions from the Monitoring Trends in Burn Severity (MTBS) dataset [4], each affected by wildfires in California during 2021. TESSERA embeddings for 2021 were obtained and UMAP dimensionality reduction was applied to a random subsample of pixels. Fire boundaries and burn severity data were sourced from the dataset. The resulting UMAP projections demonstrated strong separability in two-dimensional space, visually highlighting TESSERA’s capacity to detect disturbances at the pixel level. Burn Area A experienced two distinct wildfires—in June and August—while Burn Area B underwent a single large fire that affected mostly forested areas, resulting in a heterogeneous severity of the burn. The UMAP revealed separability across three domains (Fig. 5):

- **Burned area detection:** In both regions, burned pixels formed distinct clusters from unburned, with a clearer separation in Burn Area A.
- **Temporal fire differentiation:** In Burn Area A, embeddings separated pixels burned in June vs. August, suggesting temporal sensitivity to disturbance events.
- **Burn severity gradient:** In both regions, a gradient structure in the UMAP space corresponded to burn severity, indicating that TESSERA encodes the magnitude of the disturbance.

Because TESSERA encodes an annual time series of spectral and radar signals for each pixel, it inherently captures changes in pixel trajectories without requiring prior preprocessing or the selec-

tion of cloud-free before-and-after images. This capacity supports a simplified, scalable pipeline for monitoring large-area disturbances.

2.5 Stocking indices in voluntary carbon markets

The conversion of degraded pastures into species-rich agroforestry systems has the potential to increase carbon sequestration while minimizing leakage liabilities [110]. To fund the transition, project developers can participate in the voluntary carbon market (VCM), but need to monitor above-ground biomass (AGB) over potentially large areas. This is a costly and inefficient undertaking if it is done only by field sampling.

To enable cost reductions, the most widely applied standard in the VCM (VM00047 from Verra [155]) allows project promoters to use remotely quantified 'stocking indices' to assess project performance between 5-yearly ground truth assessments; project developers merely need to demonstrate that the chosen stocking index is correlated with the AGB. Upon acceptance, project developers can use the index to quantify the additionality of the project and to assess the performance of the project.

Here, we evaluate a simple TESSERA-derived stocking index against five widely used globally-available canopy height and AGB products that are often used in the VCM. To derive the stocking index from the TESSERA embeddings, GEDI relative height differences between RH95 and RH10 were used as target values for a pixel-wise RF regression following the methodology outlined in Atzberger et al. [13]. Without further fine-tuning, the derived stocking index, as well as five other state-of-the-art canopy height and AGB products (see [1] for details), were individually rescaled so that their regression lines best matched (i.e., with slope 1 and zero bias) *in situ* data collected at 38 agroforestry sites in Para State, Brazil. This rescaling ensures a fair comparison between the various products.

A comparison of R2 and RMSE demonstrates that the TESSERA-derived stocking index consistently outperforms alternative products (Figure 6). As the alternative stocking indices all use similar (optical and microwave) inputs to derive canopy height, respectively, AGB, the superior performance of the TESSERA-derived stocking index must be attributed to the efficiency of the TESSERA embeddings.

3 Conclusion

In this work, we introduce TESSERA, an innovative Remote Sensing Foundation Model that provides ready-to-use embeddings with worldwide coverage at 10-meter resolution through self-supervised learning applied to pixel-level optical and microwave satellite time series data. TESSERA embeddings establish new performance standards, while our open-source methodology and GEOTESSERA library permit use of our work even by non-specialists who lack access to high-performance computing. We evaluated TESSERA's capabilities across five distinct tasks, benchmarking our approach against leading task-specific models and existing foundation models. Our findings demonstrate that TESSERA surpasses both conventional RF baselines and current state-of-the-art geospatial foundation models in these diverse downstream applications.

Acknowledgments

We gratefully acknowledge help from AMD Inc., Tarides, Jane Street, the Dawn supercomputing team at Cambridge, the Aalto University Science-IT project and the Aalto Scientific Computing team, and the UKRI STFC AIRR Programme for providing us access to compute resources.

Funding: ZF and SK were funded by a charitable donation made by Dr Robert Sansom to the University of Cambridge. SJ was funded by a charitable donation from John Bernstein. SS received funding from the Jenny and Antti Wihuri Foundation and the Helsinki Institute for Information Technology.

Author contributions: TESSERA conceptualization: CA
System design: CA, ZF, SJ, SK

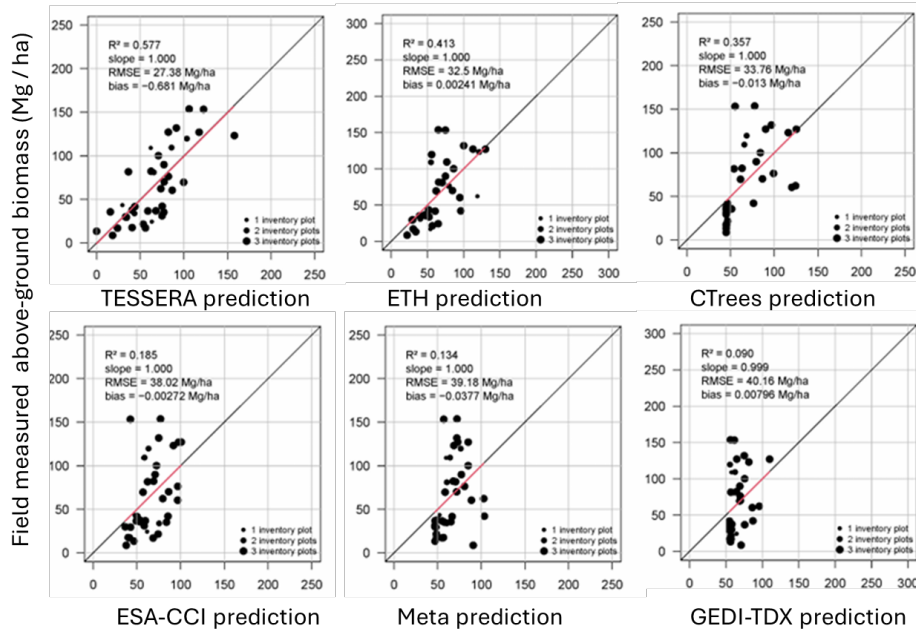


Figure 6: TESSERA outperforms various stocking indices commonly used in the Voluntary Carbon Market. Comparison of in-situ AGB measurements in 38 agro-forestry plots in Para State, Brazil with TESSERA (top left) and five other remote sensing products (see [1] for details). Note that the different products were originally provided in different units and converted to AGB as follows: (a) TESSERA: difference in relative heights of GEDI estimates of RH90 and RH10 converted to AGB using $15.502 X + 160.5$; (b) ETH canopy height converted using $3.4 X$; (c) CTrees canopy height converted using $1.806 X + 44.9$; (d) ESA AGB converted using $0.407 X + 34.0$; (e) Meta canopy height converted using $3.723 X + 46.6$; (f) GEDI-Tandem-X AGB prediction converted using $0.3 X + 54.3$. Details on the conversion functions are provided in Supplemental section I.

System implementation: ZF, RY, MCL, AM
 Data curation: ZF, RY, JK, SJ, AM, DAC, SK
 Downstream tasks: MCL, CA, SS, DAC, CA, MI, ZF, JK
 Paper conceptualization: SK, AM, DAC, AB, SJ
 Paper draft: ZF, MCL, RY, SS, SK, JK
 Paper review and refinement: AB, CA, DAC, SJ, SK

Competing interests: There are no competing interests to declare.

Data and materials availability: Our framework integrates openly available data from the Copernicus Sentinel-2 (S2) [47] optical and Sentinel-1 (S1) [46] SAR missions, leveraging the strengths of each sensor. We used S2 Level-2A surface reflectance products, providing detailed spectral information across 10 bands (Red, Blue, Green, NIR, NIR8, Red-edge1, Red-edge2, Red-edge3, SWIR16, and SWIR22). To remove cloud contamination, we filtered the time series using the associated Sen2Cor scene classification map to mask cloudy observations. For SAR data, we processed Sentinel-1 Ground Range Detected imagery to derive calibrated backscatter coefficients in VV and VH polarizations, applying standard corrections using the ESA SNAP toolbox [48].

The Google Satellite Embedding V1 dataset [56] is licensed under CC-BY 4.0 and is produced by Google and Google DeepMind.

PRESTO embeddings can be created on demand in Google Earth Engine [57] using VertexAI [58].

Our global embedding map—initially for 2024 and eventually one for each year from 2017 to 2024—is ~250 TB and is freely available for download, along with the parameters of the TESSERA model, the code to retrieve Sentinel-1 and Sentinel-2 data, and the training and inferencing code [152]. To allow for the seamless use of our embeddings in existing geospatial workflows, we have released the GEOTESSERA Python library into the PyPI repository [124], which is the official third-party software repository for Python. This library automates the retrieval of TESSERA embeddings for a given year and geographical region, merging them into a numpy buffer [62] that can be passed directly into downstream tasks. The embeddings themselves are checksummed and indexed using Pooch [151] to check data integrity and handle retrieval.

The crop type identification downstream task uses the open INVEKOS Austrian crop dataset [3].

The burn area detection task uses the open Monitoring Trends in Burn Severity (MTBS) dataset [4].

The canopy height downstream task uses open access airborne laser scan data collected in the Danum valley and Sepilok [33].

The AGB downstream task uses the open BioMassters dataset [111].

The stocking index downstream task uses plot data from 38 plots in Brazil. This contains private information regarding plot owners, hence data access will require a Data Transfer Agreement.

A Model details

Our input data consists of Sentinel-2 optical satellite imagery (Level-2A bottom-of-atmosphere) and Sentinel-1 Synthetic Aperture Radar (SAR, Radiometrically Terrain Corrected).

A.1 Data Representation

We consider remote sensing data [46, 47] with C channels (spectral bands or polarizations). Each data tile R_t at time t is represented as a 3D array with dimensions:

$$R_t \in \mathbb{R}^{W \times H \times C} \quad (1)$$

where W is the width (longitude dimension), H is the height (latitude dimension), and C is the number of spectral channels.

Each tile is accompanied by a corresponding binary mask V_t of dimensions:

$$V_t \in \{0, 1\}^{W \times H} \quad (2)$$

where $V_t(i, j) = 0$ indicates clouding or missing data for the pixel at spatial coordinates (i, j) , and $V_t(i, j) = 1$ indicates valid data.

A.2 Temporal Data Stacking

We stack spatially aligned tiles over a time period that spans T time steps ($t = 0, 1, \dots, T - 1$). The temporal data stack is defined as:

$$\mathbf{D} = [R_0, R_1, \dots, R_{T-1}] \quad (3)$$

$$\mathbf{M} = [V_0, V_1, \dots, V_{T-1}] \quad (4)$$

A.3 Time Series Extraction and d-pixel Definition

For a given spatial location (i, j) and spectral channel c , the time series $S_{i,j,c}$ represents all channel c values at coordinates (i, j) over the entire time period:

$$S_{i,j,c} = [R_0(i, j, c), R_1(i, j, c), \dots, R_{T-1}(i, j, c)] \quad (5)$$

We define a *d-pixel* $P_{i,j}$ as the collection of all spectral channels by timesteps at a given spatial location (i, j) :

$$P_{i,j}(c) = S(i, j, c) \quad (6)$$

In other words, the d-pixel provides all spectral values (Sentinel-2) or backscatter values (Sentinel-1) at a given point over time. Note that d-pixels can be sparse and are accompanied by a mask vector $m_{i,j}$ of size T that indicates the timesteps for which there is valid data, with a value 1 indicating that the corresponding row in $P_{i,j}$ is valid.

A.4 The d-pixel Representation

We represent each 10-m pixel in the time series of images from annual multi-spectral (Sentinel-2) and SAR backscatter (Sentinel-1) as a “d-pixel” array (see Fig. 1 a). In this array, each row corresponds to a chronologically ordered observation date, and each column is a specific spectral band or polarization. This representation accommodates data gaps encountered in remote sensing due to cloud cover (for optical data) or other atmospheric interference and acquisition irregularities. Observations identified as invalid (e.g., via Sentinel-2 scene classification layers for clouds, or missing Sentinel-1 acquisitions) are masked and are handled by downstream model components,

Table 1: Variable definitions for remote sensing data structure

Variable	Dimensions	Description
R_t	$W \times H \times C$	Remote sensing data tile at time t
V_t	$W \times H$	Binary mask for tile at time t (1=valid, 0=invalid/clouded)
\mathbf{D}	$T \times W \times H \times C$	Complete temporal data stack
\mathbf{M}	$T \times W \times H$	Complete temporal mask stack
$S_{i,j,c}$	$T \times 1$	Time series for channel c at location (i, j)
$P_{i,j}$	$C \times T$	d-pixel: all spectral channels by timesteps at location (i, j)
$m_{i,j}$	$T \times 1$	d-pixel mask indicating valid timesteps at location (i, j)
W, H	Scalar	Spatial dimensions (width, height)
C	Scalar	Number of spectral channels + polarizations
T	Scalar	Number of time steps

for instance, by being ignored during attention computation or ignored in the temporal sampling process.

A.5 Dual-Encoder Architecture

Given the distinct nature of Sentinel-1 SAR and Sentinel-2 MSI data, TESSERA employs two separate, parallel Transformer-based encoder branches.

- **Sentinel-2 MSI Encoder:** This branch processes a time series of 10 spectral bands (excluding the 60 m bands used for the detection of water vapor and clouds) from Sentinel-2. We used blue (B2), green (B3), red (B4), red edges 1–3 (B5, B6, B7), near-infrared (B8, B8A), and shortwave infrared (B11, B12).
- **Sentinel-1 SAR Encoder:** This branch processes a time series of 2 polarizations from Sentinel-1 (VV and VH).

Each encoder begins by linearly embedding the input features (spectral bands or polarizations) for each time step. To preserve sequence order and incorporate temporal context, learnable positional encodings based on the Day-of-Year (DOY) of each observation are added to these embeddings. The core of each encoder consists of a stack of 4 standard Transformer blocks [153], featuring multi-head self-attention and feed-forward layers to learn temporal patterns within the data streams.

To derive a single vector summarizing the entire time series for each modality, an attention-pooling layer weighs the importance of different time steps before aggregation. The resulting modality-specific embeddings (one from the S1 encoder, one from the S2 encoder) are then fused using a multi-layer perceptron.

A.6 Projector Network

The fused embedding from the dual-encoder stage is subsequently fed into a large projector network. This projector is a five-layer MLP, with each hidden layer having 16,384 dimensions. This significant expansion in dimensionality is crucial, as suggested by the original Barlow Twins work [187], to enable effective redundancy reduction during the self-supervised loss computation. The final output of the projector for each input d-pixel is an embedding, which is then used in the loss calculation. For downstream tasks, we use the 128-dimensional output from the fusion MLP (before the projector) as the final pixel embedding. The TESSERA encoder (up to the fusion MLP) has approximately 46 million parameters, while the projector accounts for the majority of the model’s ~ 1.4 billion parameters.

Table 2: Architectural parameters of the TESSERA v1.0 model.

Component	Parameters	Percentage of Total
Encoder (Feature Extractor)	45,697,026	3.29%
Sentinel-1 Encoder	22,846,465	1.64%
Sentinel-2 Encoder	22,850,561	1.64%
Fusion MLP	131,200	<0.01%
Projector (for Training only)	1,344,700,421	96.71%
Total Parameters	1,390,528,647	100.00%

A.7 Self-Supervised Training

A.7.1 Augmented View Generation

The TESSERA model is trained using a modified Barlow Twins objective function [187]. For this objective, two distorted views, denoted as Y_A and Y_B , are generated for each input d-pixel. In TESSERA, these views are created by independently running the temporal sampling and preprocessing pipeline twice for the Sentinel-1 and Sentinel-2 data associated with a given d-pixel. This process involves:

1. For each view, independently sampling a fixed number of valid observation dates from the annual Sentinel-2 time series (10 spectral bands).
2. For each view, independently sampling a fixed number of valid observation dates from the annual Sentinel-1 time series (2 polarizations).

These views represent different, valid, but inherently incomplete glimpses of the pixel’s true temporal-spectral evolution, akin to observing the same location through intermittent cloud cover or from different satellite passes at different times. The model learns by reconciling these partial views. The inherent differences between the Sentinel-1 SAR and Sentinel-2 MSI modalities further provide diverse perspectives on the same underlying physical processes. Thus, our augmentations are fundamentally about sampling from the available, inherently incomplete information streams, rather than artificially distorting a complete input.

A.7.2 Loss Function

The network processes these two views (Y_A, Y_B) through the dual-encoder and the projector to produce batch-normalized embeddings Z_A and Z_B . The standard Barlow Twins loss function, \mathcal{L}_{BT} , is defined as [187]:

$$\mathcal{L}_{BT} = \sum_i (1 - C_{ii})^2 + \lambda_{BT} \sum_i \sum_{j \neq i} C_{ij}^2 \quad (7)$$

Here, C is the cross-correlation matrix computed between the batch-normalized embeddings Z_A and Z_B . The indices i and j iterate over the dimensions of the embedding vectors. The first term (invariance term) encourages similar embeddings for different views of the same input ($C_{ii} \rightarrow 1$). The second term (redundancy reduction term) promotes information efficiency by minimizing the correlation between different embedding dimensions ($C_{ij} \rightarrow 0$ for $i \neq j$), weighted by λ_{BT} . We used the value of $\lambda_{BT} = 5 \times 10^{-3}$ as recommended in Reference [187].

To further enhance the robustness of the model and mitigate overfitting, TESSERA incorporates an additional mix-up regularization term \mathcal{L}_{MIX} , inspired by Bandara et al. [16]. This involves shuffling one set of views (e.g., Y_B) along the batch dimension to create $Y_S = \text{Shuffle}(Y_B)$, then generating mixed views $Y_M = \alpha_{mix} Y_A + (1 - \alpha_{mix}) Y_S$, where $\alpha_{mix} \sim \text{Beta}(\beta_p, \beta_p)$. The embeddings Z_M and Z_S are obtained. The mix-up loss penalizes deviations from the assumption that a linear

interpolation in the input space corresponds to a linear interpolation in the embedding space.

$$C_{target}^{MA} = \alpha_{mix}(Z_A)^T Z_A + (1 - \alpha_{mix})(Z_S)^T Z_A \quad (8)$$

$$C_{target}^{MS} = \alpha_{mix}(Z_A)^T Z_S + (1 - \alpha_{mix})(Z_S)^T Z_S \quad (9)$$

$$\mathcal{L}_{MIX} = \frac{1}{2}(\|C^{MA} - C_{target}^{MA}\|_F^2 + \|C^{MS} - C_{target}^{MS}\|_F^2) \quad (10)$$

where $C^{MA} = (Z_M)^T Z_A$ and $C^{MS} = (Z_M)^T Z_S$ are the actual cross-correlation matrices from the model’s outputs. The total loss function optimized during the training of TESSERA is a weighted sum:

$$\mathcal{L}_{total} = \mathcal{L}_{BT} + \lambda_{mix}\mathcal{L}_{MIX} \quad (11)$$

where λ_{mix} controls the strength of the mix-up regularization. We found $\lambda_{mix} = 1.0$ (as recommended by [16]) to be effective based on our experiments.

A.7.3 Pre-training Details

The TESSERA model was pre-trained using approximately 800 million d-pixels drawn from 3,012 globally distributed Military Grid Reference System (MGRS) tiles. d-pixels were generated by spatially downsampling Sentinel-1 and Sentinel-2 data by a factor of 400, i.e., selecting one pixel from each 20×20 patch. Each d-pixel contained the annual time series for 10 spectral bands of Sentinel-2 data and the annual time series of VV and VH polarizations for Sentinel-1 data.

For each pixel location, after removing invalid observations (e.g., due to cloud cover for Sentinel-2), we performed sparse temporal sampling. This involves randomly selecting a fixed number of 40 valid observation dates from the year’s data. The sequence length for the Transformer encoders was fixed at 40 timesteps for both modalities. If there are fewer than 40 cloud-free dates, replacement sampling is performed. This strategy standardizes the input sequence length and serves as a key data augmentation mechanism, building invariance to data gaps and teaching the model that the underlying signal persists regardless of the specific dates observed. Finally, these values were standardized using global statistics to stabilize training. The temporal context of each sampled observation was encoded by transforming its normalized Day-of-Year (DOY) into sine and cosine features, which were then concatenated with the corresponding spectral or backscatter measurements.

Table 3: Pre-training hyperparameters for the TESSERA v1.0 model.

Description	Symbol	Value
Optimizer & Schedule		
Optimizer	-	AdamW
Batch Size (Per-GPU)	B_{local}	2,048
Batch Size (Global)	B_{global}	32,768 (16 GPUs × 2,048)
Epochs	-	1
Base Learning Rate	η	0.002
Weight Decay	λ_{wd}	1×10^{-6}
Learning Rate Schedule	-	Linear warmup (10%), plateau (20%), cosine decay
Gradient Clipping Norm	-	2.0
Loss Function		
Barlow Twins Lambda	λ_{BT}	5×10^{-3}
Mixup Lambda	λ_{mix}	1.0
Mixup Beta Parameter	β_p	1.0
Architecture & Data		
Sequence Length	L	40
Representation Dimension	D_{repr}	128
Projector Output Dimension	D_{proj}	16,384
Quantization Bits (QAT)	-	8

As we were in a compute-limited rather than data-limited pre-training regime, we trained for a single epoch, which corresponded to approximately 6200 GPU hours on 16 AMD MI300X GPUs (192GB memory each). We used PyTorch with Fully Sharded Data Parallel (FSDP) and Automatic Mixed Precision (AMP) enabled. AdamW optimizer was used with a base learning rate of 0.002 and weight

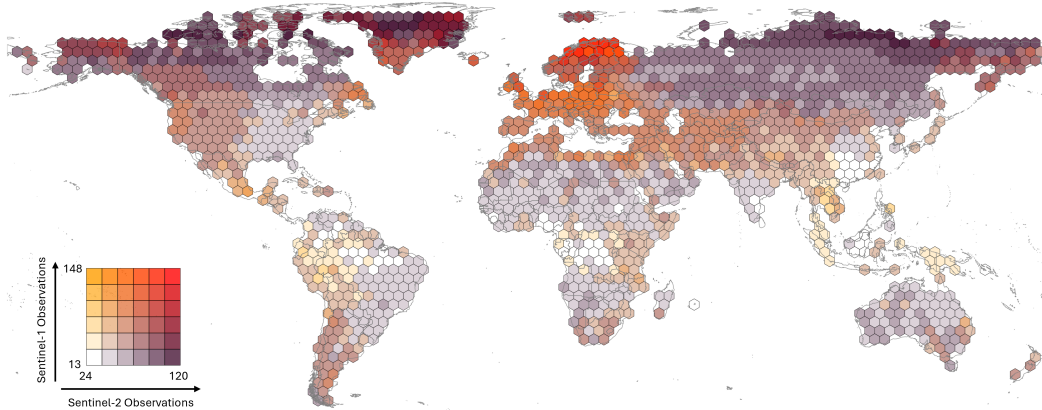


Figure 7: **TESSERA is trained on globally-distributed training data with greater data density in the northern hemisphere.** TESSERA was trained on over 3000 MGRS tiles distributed globally from 2017 to 2024. The color of each hexagon in the map corresponds to the number of valid observation days for Sentinel-1 (S1) and Sentinel-2 (S2), as defined by the bivariate color legend. This visualization highlights the density of combined S1 and S2 observations available for training across different regions, ensuring the model learns from a diverse range of geographical and environmental conditions.

decay of 1×10^{-6} . The learning rate schedule included a linear warming during the initial 10% of steps, a plateau for the next 20%, followed by a cosine decay. The global batch size was 32768.

A crucial aspect of our training methodology is a data shuffling strategy, essential for learning globally representative features from a representative sample of a vast and geographically diverse dataset. Given that d-pixels within an individual MGRS tile exhibit high spatial autocorrelation, a naive sequential or locally-shuffled data loading process would expose the model to strong geographic biases in each batch. To overcome this, we developed a custom data processing pipeline to implement a truly global shuffle across all ≈ 800 million training samples, which constituted more than 2TB of initial d-pixel data. This pipeline is conceptually illustrated in Fig. 8a.

The impact of this approach on training stability is empirically demonstrated in Fig. 8b. Compared to a conventional, localized shuffling strategy, which results in a highly volatile loss curve (top plot), our global shuffling strategy yields a markedly smoother and more stable convergence (bottom plot). This enhanced stability is fundamental for robust convergence and for preventing the model from overfitting to regional characteristics.

Operationally, the process begins with the aggregation of d-pixels from all MGRS tiles into a single, comprehensive pool. A global shuffling operation is performed on this pool, a critical step to break the spatial contiguity of data from individual tiles and ensure each training batch contains a diverse mix of geographical and environmental contexts. Following this global shuffle, the data augmentation required by the Barlow Twins framework is applied. As detailed in Appendix 5.1, this involves generating two distinct augmented views (e.g., Y^A and Y^B) for each d-pixel.

To manage the significant I/O demands of shuffling and augmenting such a large volume of data, we developed a custom high-performance pipeline that handles the reading of raw d-pixel data, executes the global shuffle, and prepares the data for augmentation. The resulting pairs of augmented d-pixels are then serialized into a compact, pickle-like file format. These files are organized into manageable chunks and loaded by PyTorch *DataLoader* workers, which stream the data and assemble the final training batches. This end-to-end pipeline ensures that each batch presented to the model is a well-shuffled, globally diverse representation of Earth’s surface characteristics, which is fundamental for training a robust pixel-wise foundation model like TESSERA.

A.8 Global Embedding Map Generation

A primary output of the TESSERA project is the generation of annual global embedding maps with 10-meter resolution for the years 2017-2024. To generate these maps, the pre-trained and frozen TESSERA dual encoder (excluding the projector) is used. For each 10-meter pixel on the globe and for each year:

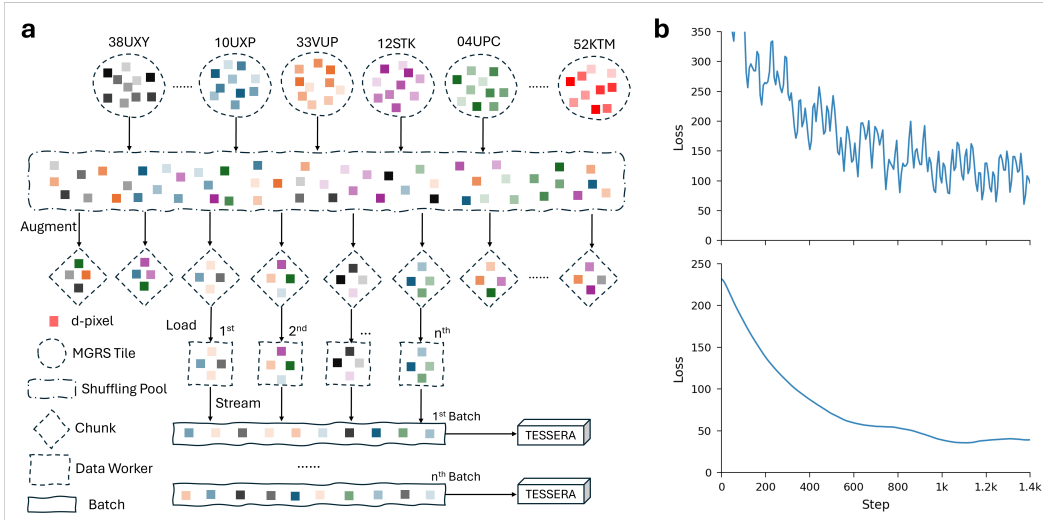


Figure 8: Data shuffling greatly improves training stability. **a**, Schematic of the data shuffling and loading process. D-pixels (colored squares) from thousands of MGRS tiles are first aggregated into a global pool. A custom Rust binary [152] performs a global shuffle on this multi-terabyte dataset before applying augmentations. The processed data is then organized into chunks and streamed by data workers to form well-shuffled, globally diverse training batches. **b**, Comparison of training loss curves. The top plot shows the volatile loss progression typical of a localized shuffling strategy, which is susceptible to geographic bias. The bottom plot shows the significantly smoother and more stable loss curve achieved with our global shuffling pipeline, demonstrating more effective and robust model convergence.

1. The full Sentinel-1 and Sentinel-2 time series data at 10-meter resolution are acquired and preprocessed to form d-pixels. Unlike pre-training, no spatial downsampling is performed at this stage.
2. A fixed number of 40 timesteps is sampled from the valid observations within the year for both Sentinel-1 and Sentinel-2 data, along with their DOY positional encodings.
3. These sampled time series are fed into their respective frozen TESSERA encoders.
4. The outputs from the S1 and S2 encoders are fused by the MLP, producing a 128-dimensional embedding vector for that pixel for that year.

This process is repeated for all land pixels globally to create an annual embeddings map of shape $(H, W, 128)$, where H and W are the dimensions of the global 10-meter grid.

B Scaling with data and network size

To identify an optimal and efficient architecture for TESSERA, and to understand the scaling properties of our model, we conducted a series of experiments using the Austrian crop classification task as the downstream task. Our investigation focused on two main areas: the impact of the projector network’s dimensions and the overall model scaling laws concerning performance versus computational cost (Fig. 9).

Our experiments revealed that the performance of the final embeddings on the chosen downstream task of crop classification in Austria was relatively insensitive to the size of the Transformer encoders. We found that using 4 transformer layers, each with 4 attention heads, provided a strong baseline without incurring excessive computational overhead during inference. This makes the feature-extracting part of the model computationally efficient.

In contrast, the architecture of the projector network proved to be critical for effective self-supervised learning. We performed a parameter sweep over the projector’s depth (number of layers) and width

(number of neurons per layer), with results shown in Fig. 9a. As discussed by Zbontar et al. [187], deeper and wider projectors consistently improved performance, as measured by the validation F1 score in the downstream task. The highest validation score was achieved with the largest configuration tested (8 layers deep, 32,768 neurons wide). However, this configuration led to an out-of-memory error with our standard global batch size; therefore, we halved the batch size to 4096 to enable stable training for this specific setup, indicated by the dagger symbol (†) in the figure. For the final TESSERA v1.0 model, we selected the configuration with 4 layers and a width of 16,384, marked with a star (*), as it provided a strong balance between high performance and computational efficiency.

Furthermore, we analyzed the relationship between model performance, the number of trainable parameters, and the total training computation (FLOPs), as shown in Fig. 9b. The results demonstrate a clear scaling trend: model performance improves predictably with increases in model size and computational budget. This confirms that TESSERA’s performance can be further enhanced with greater computational resources, following established scaling laws for large neural networks. The final TESSERA v1.0 model is marked with a star (*) on this curve, highlighting its position as a model that balances state-of-the-art performance with cost-effective training requirements.

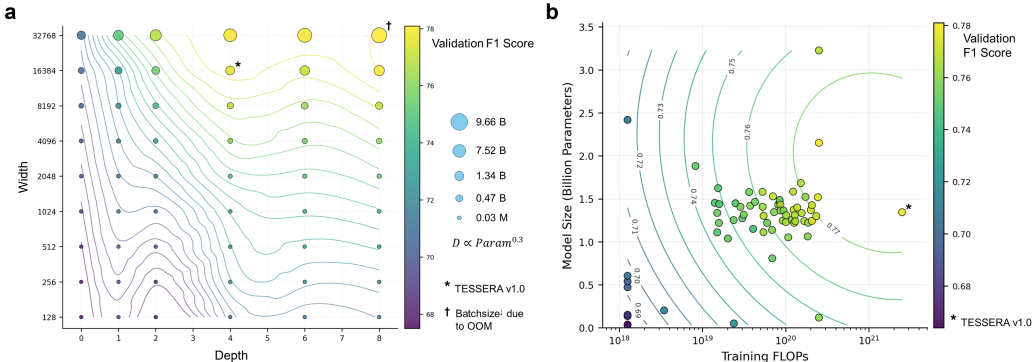


Figure 9: **Model performance improves with increasing projector size and additional computation.** **a**, Hyperparameter sweep for the projector network’s architecture. Each point represents a configuration, with its position determined by depth (x-axis) and width (y-axis). The color and size of the point indicate the validation F1 score and the number of parameters, respectively. Performance generally increases with both width and depth. The dagger (†) marks the configuration with the highest F1 score, which required a reduced batch size due to memory constraints. The star (*) indicates the final configuration selected for TESSERA v1.0, representing a balance between performance and efficiency. **b**, Scaling laws for TESSERA. The plot shows the validation F1 score as a function of training FLOPs and model size (in billions of parameters). A clear positive correlation is visible, indicating that performance improves as more computational resources and larger models are used. The final TESSERA v1.0 model is marked with a star (*) to demonstrate its position within this scaling trend.

C Ablation study

To validate the contribution of each key component within the TESSERA framework, we conducted an ablation study. We systematically removed or disabled individual components from our full model (the baseline) and evaluated the impact on the 100x downsampled Austrian crop classification dataset.

Performance was evaluated using two metrics: the standard validation overall F1 score, and a measure of the effective rank of the learned embeddings, which we refer to as the RankMe score [54]. The RankMe score quantifies the richness of the embeddings by measuring how uniformly the information is distributed across the feature dimensions. Given a batch of embeddings represented by the matrix $Z \in \mathbb{R}^{N \times D}$, where N is the batch size and D is the embedding dimension, we first compute its singular values s_1, s_2, \dots, s_D . These are normalized to form a probability distribution $p_i = s_i / \sum_j s_j$. The RankMe score is the Shannon entropy of this distribution, normalized by the

maximum possible entropy:

$$\mathcal{R}_{\text{RankMe}} = \frac{-\sum_{i=1}^D p_i \log(p_i)}{\log(D)} \quad (12)$$

A score closer to 1 indicates that the embeddings are of higher effective rank, utilizing the full dimensionality of the feature space more effectively to create richer, less redundant representations.

The results of the ablation study are summarized in Table 4. Our analysis reveals several key insights into the model’s architecture and training strategy. The most critical component turns out to be the global data shuffling pipeline, which is designed to break spatial autocorrelation and present the model with geographically diverse mini-batches. Removing mixup regularization also severely degrades results. When both are removed, the model’s performance collapses, showing that the combination of global shuffling and mixup regularization is needed to prevent overfitting and to learn generalizable, robust representations.

With removal of Sentinel-1 data, task performance decreases moderately, demonstrating some gain from the fusion of optical and SAR data yields. However, performance is still relatively good even with only Sentinel-2 data. This highlights both TESSERA’s overall robustness and its continued efficacy in regions or historical periods where Sentinel-1 data are sparse or unavailable, which is not uncommon in practice.

Finally, the effect of quantization is particularly noteworthy. We employ Quantization-Aware Training (QAT) to convert the embeddings from 32-bit floating-point (float32) to 8-bit integer (int8) format. Removing this quantization step (i.e. using full float32 precision) results in a marginal performance improvement. This demonstrates the success of our QAT strategy: we achieve a nearly four-fold reduction in the storage and bandwidth requirements for our final data products, with a negligible impact on embedding quality. This underlies our “Embeddings-as-Data” approach, making global-scale high-resolution analysis practical: Without this, each year’s embeddings would consume 1PB, making the hosting of 8 years of embedding costly and likely unachievable.

Table 4: **The ablation study demonstrates that data shuffling and mixup regularization are essential, Sentinel 1 data adds little additional value, and that quantization has nearly no impact on performance.** We study downstream crop classification performance on the 100x-downsampled Austrian crop dataset. The baseline represents the full model. Each subsequent row shows the result of removing the specified component. Performance is measured by validation F1 score and the RankMe score. Arrows (↑) indicate that higher values are better. The results demonstrate that all components contribute positively to the model’s overall performance.

Configuration	Validation F1 Score (↑)	RankMe Score (↑)
Baseline (Full Model)	0.773	0.963
w/o Global Data Shuffling	0.681	0.847
w/o Mixup Regularization	0.662	0.857
w/o Sentinel-1 Data	0.742	0.931
w/o Shuffling & Mixup	0.626	0.867
w/o Embedding Quantization	0.779	0.972

D Downstream Task Application Methodology

A core motivation for self-supervised learning with foundation models is the creation of task-agnostic feature embeddings that can be effectively transferred to various downstream tasks, particularly in scenarios with limited labeled data. Having pre-trained TESSERA on large unlabeled datasets, we evaluated the utility of its learned embeddings across different remote sensing applications. The evaluation methodology involves using pre-trained TESSERA encoders as fixed feature extractors.

The pipeline for applying TESSERA embeddings to downstream tasks is as follows (illustrated in the Supplementary Fig. 10):

1. **Download Embeddings for the Region of Interest:** The GEOTESSERA Python library [152] allows users to download embeddings for a desired region and year in the form of a numpy array.

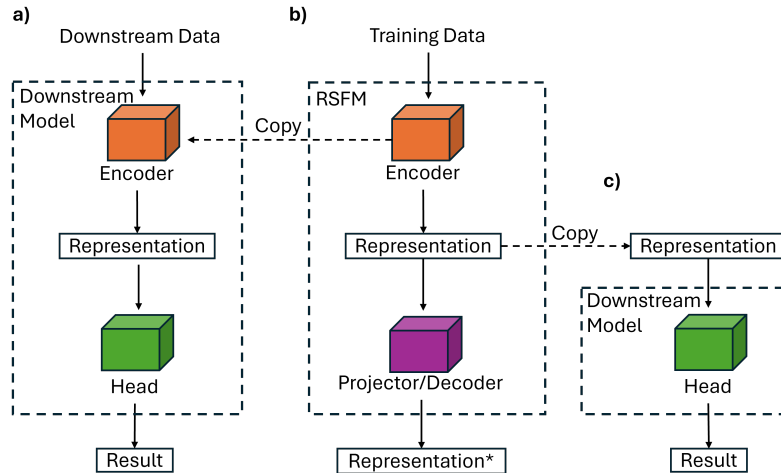


Figure 10: **Unlike common Remote Sensing Foundation Models (RSFM), TESSERA simplifies downstream task applications.** Most existing RSFMs use approach (a) where, after training, the encoder is extracted and combined with a task-specific head to form a new model for downstream tasks. Users can then fine-tune the entire model or only the head. Another approach (b) is where both the encoder and the projector (or decoder) are typically updated. In contrast, the TESSERA approach (c) uses pre-generated embeddings directly as input. This results in lightweight downstream models that consist only of a task-specific head.

2. **Prepare Labeled Downstream Data:** The labeled dataset for the target task (e.g., pixel-level crop-type labels, canopy height measurements, or land use change polygons) is prepared.
3. **Design Task-Specific Head:** A lightweight, task-specific neural network module (the "head") is designed. This head takes the extracted TESSERA embeddings as input.
 - For pixel-wise classification (e.g., crop classification), the head is typically a shallow MLP (1-3 layers) ending in a softmax output layer.
 - For pixel-wise regression (e.g., canopy height regression), the head is usually an MLP ending in a single linear output neuron.
 - For tasks requiring spatial context from the embeddings (e.g., canopy height mapping over an area, semantic segmentation), the input to the head can be a patch of TESSERA embeddings (e.g., $64 \times 64 \times 128$). The head might then be a convolutional architecture, such as a UNet, that processes these spatial feature maps to produce dense predictions.
4. **Train Downstream Head:** Only the parameters of this newly defined task head are trained using the extracted TESSERA embeddings as input features and the corresponding labels. Standard supervised learning techniques, optimizers (e.g., Adam), and task-appropriate loss functions (e.g., Cross-Entropy for classification, Mean Squared Error for regression) are used. This training typically requires significantly less labeled data and computational power compared to training a deep model from scratch.
5. **Evaluation:** Once the head is trained, inference is performed on a test set by extracting TESSERA embeddings for the test samples and passing them through the trained head. Performance is evaluated using standard metrics relevant to the task.

This workflow allows the use of TESSERA embeddings in a range of diverse applications, demonstrating its role as a foundational model for geospatial analysis.

TESSERA users who would like to generate their own embeddings can load the frozen weights from the saved pre-training checkpoint into the TESSERA dual encoder architecture. For each input sample (e.g., pixel, object, or patch) in the region of interest, its corresponding Sentinel-1 and Sentinel-2 time series data for the relevant year must be downloaded and processed using the d-pixel creation pipeline. These d-pixels are passed through the frozen encoders and their outputs

are fused by the MLP to generate the final 128-dimensional TESSERA embedding for that sample. To enhance stability, multiple embeddings can be created with different random temporal samples and averaged.

E Downstream Task: Austrian Crop Classification

E.1 Dataset and Preprocessing

We used the publicly available INVEKOS dataset for Austria, focusing on the 2022 growing season [3]. The data set originally contained 154 crop types, which we grouped into 17 broader classes (for example, combining sugar beet and feed beet) based on phenological similarity and sample availability to ensure robust training and evaluation. For each pixel in the dataset, we extracted its corresponding 128-dimensional TESSERA embedding from our generated 2022 global embeddings map.

E.2 Pixel-wise Classification Baselines

To provide a comprehensive performance comparison, we implemented three distinct models for pixel-wise classification:

- **TESSERA + MLP:** The primary model, where the frozen 128-dimensional TESSERA embeddings were used as input to a simple MLP. The MLP consisted of two hidden layers with 256 and 128 neurons, respectively, using ReLU activation functions, followed by a softmax output layer for the 17 classes.
- **PRESTO + MLP:** For a direct and fair comparison with a leading foundation model, we used the official pre-trained PRESTO model [149] to generate its pixel embeddings. These embeddings were then fed into an MLP head identical to the one used for TESSERA.
- **GSE + MLP:** To include another key foundation model, we used the publicly available Google Satellite Embedding (GSE) V1 dataset [56]. These embeddings were similarly fed into an MLP head identical to the one used for TESSERA.
- **Random Forest:** As a traditional baseline, we trained a Random Forest (RF) classifier directly on raw time-series data. For each pixel, we utilized all available Sentinel-1 (2 polarizations) and Sentinel-2 (10 spectral bands) observations throughout the year. The temporal and spectral/polarization dimensions were flattened and concatenated to form a single 1256-dimensional feature vector. The RF model consisted of 200 trees, with other parameters set to standard values.

For the experiments shown in the main text’s figure, we trained these models on randomly selected subsets of the data (from 1% to 30% for panel a; specified samples-per-class for panel b), using a fixed validation set for hyperparameter tuning and a held-out test set for final evaluation.

E.3 Patch-wise Semantic Segmentation

To assess spatial-contextual performance, we conducted a semantic segmentation experiment. The approach varied based on the foundation model’s architecture:

- For the foundation models capable of generating pixel-wise embeddings, namely **TESSERA**, **PRESTO** [149], and **GSE** [56], a distinct workflow was used. We first construct patches from their pixel-level embeddings (e.g., a data cube of size $H \times W \times C$). These patches were then fed into a standard **UNet** architecture [128], which learns to model the spatial relationships between the embeddings to produce a segmentation map. It is noteworthy that while TESSERA and PRESTO’s base embeddings do not explicitly model spatial context, GSE’s do. However, their shared ability to generate pixel-level outputs makes them suitable for this UNet-based downstream approach.
- For other foundation models that are inherently patch-based (e.g., Prithvi [141], Satlas [18]), their encoders already process image patches. Therefore, for these models, we only attach and train a **UPerNet decoder head** to their encoders to generate the final segmentation output. We did not freeze the encoders during the finetuning.

Performance was measured using mean Intersection over Union (mIoU) and macro F1 scores. A visual comparison for example patches is provided in Supplementary Fig. 11.

E.4 Embedding Space Analysis

The 2D visualizations shown in the main text (Figure 2 d) were generated by applying the Uniform Manifold Approximation and Projection (UMAP) [103] algorithm to the embeddings of every pixel within the Austrian study area. UMAP is a non-linear dimensionality reduction technique based on Riemannian geometry and algebraic topology. It constructs a weighted k-nearest neighbour graph in the original high-dimensional space, then optimizes a low-dimensional projection to primarily preserve local distances and local structure. UMAP, like other non-linear techniques such as t-SNE and LargeVis, is designed to preserve local relationships within high-dimensional data; however, it is also able to retain more of the global structure, making it particularly effective for understanding both fine-scale and broader patterns in the embedding space. In this work, the entire embeddings map (e.g., an array of shape $H \times W \times 128$, where H and W are the height and width of the region) was used as a direct input to UMAP for TESSERA, PRESTO, and GSE embeddings.

To quantitatively measure the quality of the clustering in the original 128-dimensional space, we calculated the Silhouette score and the Davies-Bouldin Index.

- The **Silhouette score**, $s(i)$, for a single data point i measures how similar it is to its own cluster compared to other clusters. It is defined as:

$$s(i) = \frac{b(i) - a(i)}{\max(a(i), b(i))} \quad (13)$$

where $a(i)$ is the mean distance between i and all other points in the same cluster, and $b(i)$ is the mean distance from i to all points in the nearest neighboring cluster. The score ranges from -1 to 1, where a high value indicates that the object is well matched to its own cluster and poorly matched to neighboring clusters.

- The **Davies-Bouldin Index** (DBI) evaluates clustering quality by computing the ratio of within-cluster scatter to between-cluster separation. For a set of k clusters, it is defined as:

$$\text{DBI} = \frac{1}{k} \sum_{i=1}^k \max_{j \neq i} \left(\frac{\sigma_i + \sigma_j}{d(c_i, c_j)} \right) \quad (14)$$

where σ_i is the average distance of all points in cluster i to their centroid c_i , and $d(c_i, c_j)$ is the distance between the centroids of clusters i and j . Lower DBI values indicate better clustering, with a score of 0 representing the ideal case where clusters are compact and well separated.

F Downstream Task: Canopy height estimation

F.1 Study Areas and Ground Truth Datasets

Canopy height prediction was evaluated in a 5×6 km area in the Danum Valley, Borneo. This region is covered in tropical rainforest dominated by the fast-growing dipterocarp family, which hosts some of the tallest trees in the tropics [135, 120]. Ground truth data was derived from airborne laser scanning (ALS) performed in February 2020 [33]. ALS data provides detailed 3D point clouds of vegetation and terrain structure, which were processed using the LSPKIFREE algorithm [51] to estimate top-of-canopy height at 1 m resolution. These canopy height rasters were then downsampled using mean pooling to 10 m to match the resolution of the TESSERA representations.

F.2 Modeling Methods

To predict the canopy height from the different embeddings, we used a standard U-Net architecture [128]. It takes as input a 32×32 pixel patch (covering a 320×320 m area) of representations. For 128-dimensional embeddings (as in TESSERA and PRESTO), this results in a $32 \times 32 \times 128$ data cube. The network outputs a single-band 32×32 raster of predicted canopy height values. The

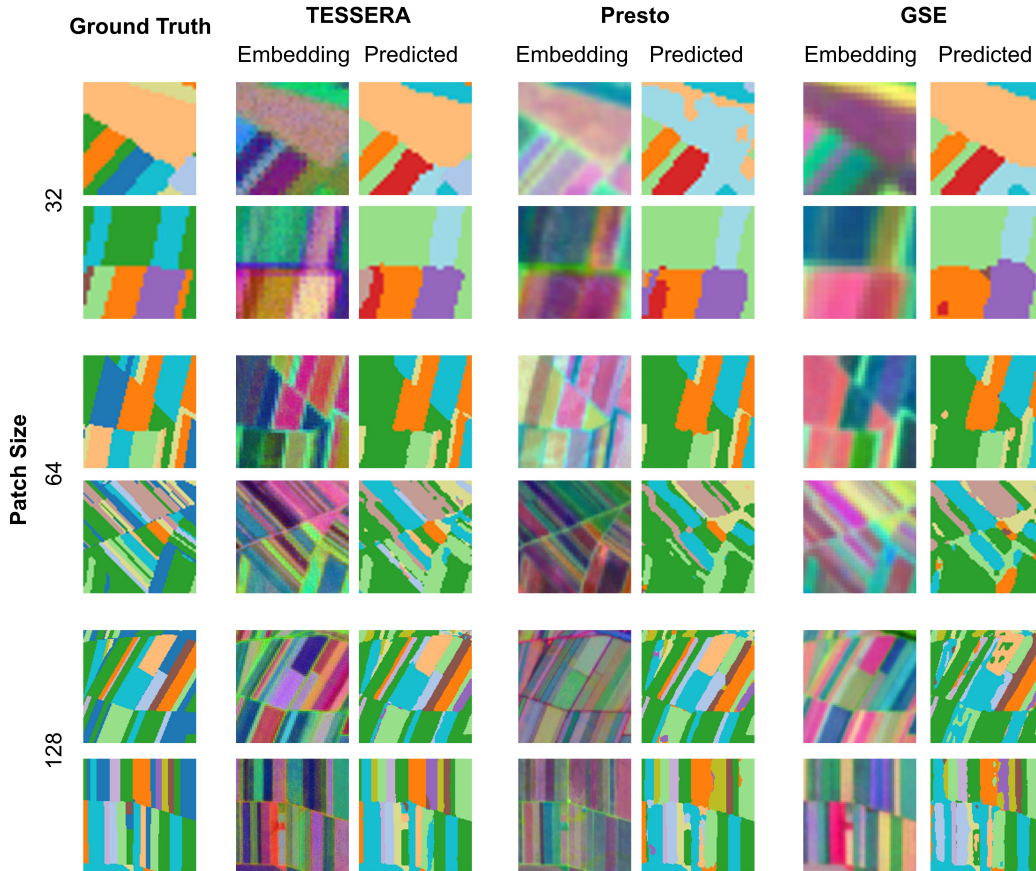


Figure 11: **TESSERA predictions most closely resemble the ground truth for patch-based semantic segmentation.** Each row corresponds to a different patch size (32x32, 64x64, 128x128). The first column shows the ground truth segmentation. For each model (TESSERA, Presto, and GSE), two columns are displayed: a PCA visualization of the input embeddings for the patch (labeled 'Embedding') and the final predicted segmentation map (labeled 'Predicted').

proposed U-Net contains approximately 30 million parameters and was trained for 200 epochs using a batch size of four patches. At the end of each epoch, the model was evaluated using validation data and the model with the best performance on the validation set was retained for the final evaluation. In practice, training usually converged within the first 20 epochs, with rare boosts in performance later in training. Model training was done in Python using PyTorch.

To ensure spatial generalization and avoid overfitting local patterns, the reference data were divided into training, validation, and test sets that are spatially disjoint. Each study region was divided into four spatial folds based on cardinal directions (bottom, top, left, right), each fold covering 50% of the area. For each fold, the remaining half of the region was used for training and validation. To account for inherent model randomness, we trained three independent models per fold, resulting in 12 trained models for each foundation model. This strategy captures variability due to both spatial heterogeneity and training randomness. The final performance of the model was evaluated on the test data held using the following metrics: coefficient of determination (R^2), root mean square error (RMSE), and mean bias.

F.3 Baselines

TESSERA, PRESTO [149], and GSE [56] embeddings were compared by training identical models using each representation as input, with all other settings held constant. Each model was trained for

200 epochs on the same data split, and the version achieving the best validation performance was selected for final evaluation on the held-out test set.

To benchmark performance against traditional remote sensing approaches, we compared the predictions against three global canopy height products: Potapov et al. [2021][121] (GLAD), Lang et al. [2023][84] (ETH), and Tolan et al. [2024][148] (Meta) as well as a regional map produced by Lang et al. [2021][85]. These maps were downloaded at 10 m resolution from Google Earth Engine and compared directly to the canopy height derived from ALS. Although there are some temporal mismatches between ALS acquisition (2020) and global products, we assume relative stability of canopy height in the short term in this region.

Finally, we trained the U-Net model using Sentinel-2 input as a baseline. This approach retained the same model architecture, patch size, and evaluation setup, but replaced embeddings with cloud-free annual median composites of Sentinel-2 imagery. Cloud masking and compositing were performed in GEE, resulting in 12 channel input images (band XYZ excluded), with one channel for each Sentinel-2 spectral band. Although different Sentinel-2 bands have different spatial resolutions, all were resampled to 10 m to match the FM pipelines.

G Downstream Task: Burned area detection

G.1 Study Areas and Ground Truth Datasets

For fire disturbance detection, two 15×15 km tiles in California were selected at random from the pool of training samples in the burn scars benchmarking dataset [76], referred to as Burn Area A and Burn Area B. Burn Area A comprises a heterogeneous landscape of forest, shrubland, agricultural land, and built infrastructure. In 2020, it experienced two separate wildfires: the 'Quail Fire' in June (~ 730 ha) and the much larger 'Hennessey Fire' in August ($\sim 121,000$ ha). Burn Area B experienced a single large fire 'Glass' ($\sim 27,500$ ha) in September 2020 that primarily affected forested land. In all cases, most of the impact of the fire occurred in vegetated areas composed of forest and shrubland. To classify the dominant land cover types in the burn areas, we used the Dynamic World Land Cover data set [2].

The dataset from the Monitoring Trends in Burn Severity (MTBS) program [4] was used to identify burned areas and burn severity. Fire ignition and containment dates, as well as fire perimeters, were obtained from the MTBS burned area boundaries dataset. Burn severity—defined as the measure of ecological damage caused by fire [55]—was derived from categorical and continuous severity metrics provided by MTBS. To obtain burn severity categories of low, medium and high, as well as continuous burn severity, we used MTBS burn severity annualized dataset as well as individual severity maps for each fire. MTBS calculates severity using two primary indices: the differenced NBR (dNBR) and its relativized form (RdNBR), both calculated from pre- and post-fire Landsat images. Low severity typically indicates limited ecological impact, while high severity reflects significant ecological disruption and vegetation mortality [55]. Since MTBS datasets are derived from Landsat, they are provided at 30-meter resolution, and were upsampled to 10-meters to match the resolution of TESSERA representations. The MTBS and Dynamic World datasets were downloaded as 10 m rasters from Google Earth Engine [57].

G.2 Dimensionality Reduction

We used UMAP (Uniform Manifold Approximation and Projection) [103] to reduce 128 dimensions of TESSERA embeddings to 2D for visual inspection of FM representations in areas affected by wildfires. We applied the dimensionality reduction to 128-dimensional TESSERA embeddings and visualized the resulting 2D projections. To interpret the structure of the projected clusters, we colour coded points according to different annotation schemes: burn state (burned vs. unburned), land cover class, or burn severity. These visualizations helped us assess whether FM embeddings spatially separate ecological conditions of interest. Each Burn Area contains over two million 10-meter pixels. To reduce computational cost and improve legibility, we randomly subsampled a subset of pixels prior to applying the dimensionality reduction. UMAP projections were additionally used to classify pixels into unburned, low, moderate, and high-severity classes using a random forest (RF) classifier, to quantify the separability in the UMAP embedding space. UMAP projections

were computed using the UMAP-LEARN Python library and RF was implemented using the SCIKIT-LEARN Python library.

H Downstream Task: Above-ground biomass estimation

H.1 Dataset

For the AGB regression task, we used the ground truth data from the Biomasssters dataset [111]. Patch coordinates and collection years [111] were used to retrieve satellite imagery to generate TESSERA and Google Satellite Embeddings (GSE) [56].

For the SpectralGPT baseline, we used the preprocessed satellite data from the Biomasssters dataset as input, since the codebase for SpectralGPT [67] did not include a preprocessing pipeline at the time of our analysis.

H.2 UNet model architecture

To obtain AGB estimates, we trained a convolutional neural network based on a UNet architecture [128], using TESSERA or GSE embeddings [56] as input representations. The model received $128 \times 256 \times 256$ and $64 \times 256 \times 256$ input patches for TESSERA and GSE, respectively, where the first dimension denotes the number of channels.

The network followed a standard UNet structure with two encoder and decoder stages. The encoder comprised two convolutional blocks with 256 and 512 channels, each consisting of two 3×3 convolutions followed by batch normalization, ReLU activation, and 2×2 max pooling. A 1024-channel bottleneck block was used prior to upsampling. The decoder mirrored the encoder, using transposed convolutions for upsampling and skip connections from the encoder, followed by double convolution blocks. A final 1×1 convolution produced the single-channel regression output. The model had approximately 30 million trainable parameters. The loss function was defined as the root mean squared error (RMSE) averaged over individual patches.

Training was performed with the Adam optimizer (learning rate = $1e-4$, batch size = 4). Finetuning on the full dataset (80% training / 20% validation) using a single NVIDIA H200 GPU and 8 CPU cores took approximately 5 hours.

H.3 Baselines

In addition to GSE, we compared TESSERA’s performance to two other baselines: the Biomasssters winner [111] and the SpectralGPT foundation model [67] combined with an UPerNet [179].

For SpectralGPT, we used the implementation provided in Ref. [101], with the Biomasssters satellite data as input and an UPerNet as the regression head. This setup was found in Ref. [101] to outperform other tested foundation models. To ensure consistency in the limited-label setting, we replaced the default sampling strategy with the same random splits used to evaluate TESSERA and normalized the inputs with their mean and standard deviation. Although we initially experimented with using per patch RMSE as the loss function to align with our evaluation metric, we ultimately reverted to the MSE loss [101] as it resulted in slightly better performance. Obtaining the results for the full dataset using a single NVIDIA H200 GPU took approximately 18 hours.

To evaluate the Biomasssters winning model, we downloaded the pre-trained model weights and ran inference on the test set. Although we attempted to retrain the model from scratch using two H200 GPUs and a different CUDA version than in the original setup, this configuration led to inferior performance compared to the original pre-trained model. According to the Biomasssters codebase, the original model was trained on two A100 40GB GPUs over the course of eight days – highlighting the greater time efficiency of TESSERA, which required only five hours.

I Downstream Task: Stocking indices in voluntary carbon markets

I.1 Relative height modeling

Participants in the voluntary carbon market can use a remotely sensed "stocking index" to quantify project additionality. The chosen stocking index must be correlated with the above-ground biomass (AGB) of the observed objects, and the strength of the correlation must be demonstrated using a suitable in situ reference dataset.

To demonstrate the superior quality of the TESSERA embeddings compared to existing state-of-the-art canopy height or AGB products, a simple stocking index was derived from GEDI relative heights and TESSERA embeddings. This permits comparing state-of-the-art models often used in the voluntary carbon market with a TESSERA-derived stocking index.

To model a suitable stocking index from the 128-dimensional TESSERA embeddings, 110,000 relative heights RH95 and RH10 from 2022 were extracted from the Sentinel-2 tile 22MCT in Para State, Brazil. From the 10 m pixel falling at the center of the full-waveform footprint, the 128 TESSERA embeddings were extracted as predictors. After data extraction, the relative height differences ($dRH = RH95 - RH10$) were used as the target variable and the 128 TESSERA embeddings as predictors. A random forest (RF) regression model with 500 trees and 42 variables per split was used to model this stocking index. To account for implausible GEDI recordings often found in areas without significant tree cover (e.g., water surfaces or agricultural fields), the dRH values of these classes were set to zero before model training. The TerraClass Amazonia 2022 land cover map [146] was used to distinguish between forest and non-forest.

For inference and assessment, the trained RF model was applied to eight Sentinel-2 tiles in the same region of Para State (MGRS tiles 22MCT, 22MCU, 22MDT, 22MDU, 22MGB, 22MGC, 22MHB, 22MHC). Within this area, a total of 38 agroforestry plots are located for which in situ measurements are available under a DTA.

I.2 Stocking index baselines

For comparison, five recent and widely used canopy height and AGB products were chosen and compared against the same set of 38 in situ AGB measurements: ETH CHM (10 m) [84], CTrees canopy tree height (5 m) [156], ESA-CCI AGB (100 m) [132], Meta CHM (1 m) [148] and GTDX AGB (25 m) [42]. Using the same shapefiles delineating the agroforestry systems, the pixels of the respective products were extracted and averaged for the chronosequence plots ($n=38$).

To ensure a fair comparison between canopy height, AGB and relative height products, the extracted averages were linearly rescaled to best correlate with in situ (AGB) data. After rescaling, all products are in units of t/ha and have an intercept of zero and a slope of one with respect to the in situ data, making their RMSE (and R^2) directly comparable.

J Interactive Habitat Mapping Tool

Here we demonstrate our interactive classification tool, a web-based utility designed for rapid human-in-the-loop habitat mapping using pre-computed model embeddings, as seen in Figure 12. The tool allows a user to first define a region of interest, for which it fetches and mosaics the relevant high-dimensional embedding tiles. To aid visual interpretation, it performs Principal Component Analysis on the embeddings and displays the first three components as a false-colour RGB image overlay on a satellite basemap.

The core of the tool is the interactive labeling workflow. A user can define custom habitat classes and provide training data by clicking on the map to place labeled points. These points and their corresponding 128-dimensional embedding vectors are used to train a k-Nearest Neighbors (kNN) classifier. The trained model then predicts a class for every pixel in the region of interest, producing a map layer that overlays a coregistered aerial view. This process allows for iterative refinement, where a user can add more points to correct misclassifications and retrain the model for immediate feedback, demonstrating an accessible method for quickly creating habitat maps without requiring deep machine learning expertise. We also provide a batch processing tool for larger regions of interest. The tools and their open source code are freely available in our github repository [152].

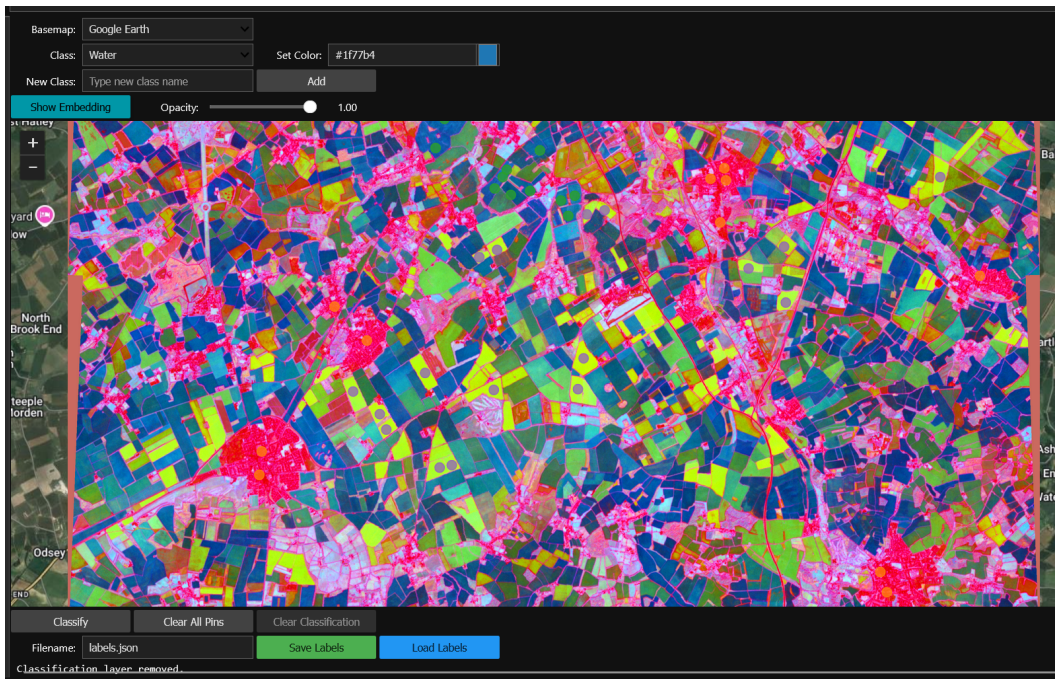


Figure 12: We provide an interactive tool to allow non-specialist users to map TESSERA embeddings to user-defined classes. We show a PCA-derived false colour map overlaid on an RGB aerial image of South Cambridge.

K Supplementary Table

The table below compares TESSERA along several dimensions with a comprehensive list of remote sensing foundation models [73].

Table 5: **TESSERA provides unprecedented ease of use, scale, and accuracy.** Unlike other remote sensing foundation models, TESSERA provides analysis-ready and gap-free outputs (R), is open (O), and provides global (G) annual (A) coverage at 10m resolution (10m). It uses spectral-temporal features (ST) at pixel level (P), is invariant to clouds (CI), provides a compressed representation (CR), is oriented to land features (LO), and includes both multispectral and radar information (MS). Codes: ✓ = Yes, ✗ = No, ? = Unknown, p = Potentially true, .. = N/A.

Foundation Model	R	O	G	A	10 m	ST	P	CI	CR	LO	MS
TESSERA (2025)	✓	✓	✓	✓	✓	✓	✓	✓	✓	✓	✓
GeoKR (2021) [87]	✗	?	✗	✗	✓	✗	✓	✗	✗	✓	✗
CVPRW (2021) [139]	✗	..	✗	✗	✓	✗	✗	✗	..	✓	✗
GASSL (2021) [14]	✗	..	✗	✗	✓	✗	✓	✗	..	✓	✗
SeCo (2021) [102]	✗	✗	✗	✗	✓	✗	✗	✗	?	✓	✗
DINO-MM (2022) [167]	✗	..	✗	✗	✓	✗	✗	✗	..	✓	✓
SatMAE (2022) [32]	✗	..	✗	✗	✓	✓	✗	p	..	p	✗
RS-BYOL (2022) [75]	✗	✗	✓	✗	✓	✓	..	✗	✓
GeCo (2022) [88]	✗	✗	..	✗	✗	✗	..	p	✗
RingMo (2022) [140]	✗	✗	✓	✗	✗	✗	?	✓	✗
RVSA (2022) [163]	✗	✗	..	✗	✗	✗	..	✓	✗
RSP (2022) [160]	✗	✗	p	✗	✗	p	✓	✓	✗
MATTER (2022) [7]	✗	✗	✓	✓	✗	✗	✓	✓	✗
CSPT (2022) [190]	✗	✗	?	✗	✗	✗	✓	✓	✗
CVPRW (2022) [133]	✗	✗	✓	✗	✗	✗	✓	✓	✓
BFM (2023) [26]	✗	✗	?	✗	✗	✗	?	✓	✗
TOV (2023) [145]	?	..	✗	✗	✓	✗	?	✗	?	✓	✗
CMID (2023) [109]	✗	..	✗	✗	✓	✗	✗	✗	?	✓	✗
RingMo-Sense (2023) [185]	✗	..	✗	✗	✓	✓	✗	✗	?	✓	✓
lal-SimCLR (2023) [122]	✗	..	✗	✗	✓	✗	✗	✗	✓	✓	✓
CACo (2023) [100]	✗	..	✗	✗	✓	✓	✗	✗	✓	✓	✗
SatLas (2023) [18]	✗	..	✓	✗	✓	✓	✗	✗	✓	✓	✗
GFM (2023) [104]	✗	..	✗	✗	✓	✗	✗	✗	✗	✓	✗
Scale-MAE (2023) [126]	✗	..	✗	✗	✓	✗	✗	✗	✗	✓	✗
DINO-MC (2023) [174]	✗	..	✗	✗	✓	✗	✗	✗	✗	✓	✗
CROMA (2023) [53]	✗	..	✗	✗	✓	✗	✗	✗	✗	✓	✓
Cross-Scale MAE (2023) [144]	✗	..	✗	✗	✓	✗	✗	✗	✗	✓	✗
DeCUR (2023) [166]	✗	..	✗	✗	✓	✗	✗	✓	✗	✓	✓
Presto (2023) [149]	✗	..	✓	✓	✓	✓	✓	✓	✓	✓	✓
CtxMIM (2023) [189]	✗	..	✗	✗	✓	✗	✗	✗	✗	✓	✗
FG-MAE (2023) [170]	✗	..	✗	✗	✓	✗	✗	✗	✗	✓	✗
Prithvi (2023) [134]	✗	..	✗	✗	✗	✓	✗	✓	✓	✓	✗
RingMo-Lite (2023) [172]	✗	..	✗	✗	✓	✗	✗	✗	✗	✓	✗
IGARSS (2023) [50]	✗	..	✗	✗	✓	✗	✗	✗	✗	✓	✗
EarthPTi (2023) [137]	✗	..	✗	✗	✓	✓	✓	✓	✓	✓	✗
USat (2023) [72]	✗	..	✗	✗	✓	✗	✗	✗	✗	✓	✗
AIEarth (2023) [182]	p	?	✓	✗	✓	✗	✗	✗	✗	✓	✗
Clay (2023) [31]	✗	..	✓	✗	✓	✗	✗	✗	✗	✓	✗
Hydro (2023) [35]	✗	..	✗	✗	✓	✗	✗	✗	✗	✗	✗
U-Barn (2023) [44]	✗	..	✗	✓	✓	✓	✗	✓	✗	✓	✗
GeRSP (2023) [69]	✗	..	✗	✗	✓	✗	✗	✗	✗	✓	✗
SwiMDiff (2023) [147]	✗	..	✗	✗	✓	✗	✗	✗	✗	✓	✗
OFA-Net (2023) [181]	✗	..	✓	✗	✓	✗	✗	✗	✗	✓	✓
SML-FR (2023) [40]	p	p	✓	✗	✓	✗	✗	✗	✗	✗	✗
Spectral-GP (2024) [67]	✗	✗	✓	✗	✓	✗	✗	✗	✗	✓	✗

Continued on next page

Foundation Model	R	O	G	A	10 m	ST	P	CI	CR	LO	MS
S2MAE (2024) [90]	×	×	✓	×	✓	×	×	×	×	✓	×
SatMAE++ (2024) [113]	×	×	✓	×	✓	×	×	×	×	✓	×
msGFM (2024) [61]	×	×	×	×	✓	×	×	×	×	✓	×
SkySense (2024) [59]	×	×	×	×	✓	✓	×	×	×	✓	✓
MTP (2024) [162]	×	..	✓	×	✓	×	✓	×	×	✓	×
DOFA (2024) [180]	×	..	✓	×	✓	×	×	×	✓	✓	✓
MMEarth (2024) [112]	×	..	✓	×	✓	×	×	×	✓	✓	✓
LeMeViT (2024) [78]	×	..	×	×	?	×	×	×	✓	×	×
SoftCon (2024) [168]	×	..	✓	×	✓	×	✓	×	×	✓	×
RS-DFM (2024) [173]	×	..	×	×	✓	×	✓	×	×	✓	×
A2MAE (2024) [188]	×	..	✓	×	✓	×	×	×	✓	✓	×
HyperSIGM (2024) [159]	×	..	✓	×	✓	✓	✓	×	✓	✓	×
SelectiveMAE (2024) [164]	×	..	✓	×	✓	×	×	×	✓	✓	×
OmniSat (2024) [11]	×	..	×	✓	✓	✓	×	?	✓	✓	✓
MM-VSE (2024) [125]	×	..	✓	✓	✓	✓	×	?	✓	✓	✓
MA3E (2024) [94]	×	..	×	×	✓	×	×	×	✓	✓	×
SpectralEarth (2024) [93]	×	..	✓	✓	×	?	×	×	✓	✓	×
SenPa-MAE (2024) [123]	×	..	✓	✓	✓	✓	✓	×	✓	✓	×
RingMo-Ae (2024) [38]	×	..	×	×	✓	×	✓	×	✓	✓	×
SAR-JEPA (2024) [89]	×	..	×	×	✓	×	×	✓	×	×	×
PIS (2024) [9]	×		✓	✓	✓
OReole-FM (2024) [39]	×	..	✓	×	✓	×	✓	×	✓	✓	×
PIEVIT (2024) [98]	×	..	✓	×	✓	×	✓	×	✓	✓	×
SatVisionTOA (2024) [138]	×	..	✓	✓	×	✓	✓	×	✓	✓	×
RS-vHeat (2024) [68]	×	..	?	?	?	?	✓	?	✓	?	✓
Prithvi-EO-2.0 (2024) [141]	×	..	✓	✓	×	✓	×	✓	✓	✓	×
AnySat (2024) [12]	×	..	✓	×	✓	×	✓	×	✓	✓	✓
WildSAT (2024) [36]	×	×	×	×	×	×	×	×	✓	✓	×
SeaMo (2024) [92]	×	×	×	×	✓	×	×	×	✓	✓	×
FoMo (2025) [22]	✓	✓	✓	×	✓	×	✓	×	✓	✓	✓
SatMamba (2025) [43]	✓	✓	×	×	×	×	×	×	×	✓	×
Galileo (2025) [150]	p	p	✓	?	✓	×	×	×	✓	✓	✓
SatDiFuser (2025)[77]	×	×	×	×	✓	×	×	×	×	✓	×
RoMA (2025) [165]	×	×	×	×	✓	×	×	×	×	✓	×
Panopticon (2025) [157]	×	✓	×	×	✓	✓	×	×	✓	✓	✓
FedSense (2025) [142]	×	×	×	×	×	×	×	×	×	✓	×
Copernicus-FM (2025) [171]	×	..	✓	×	✓	✓	×	×	✓	✓	✓
HyperFree (2025) [86]	×	..	×	×	✓	×	×	×	✓	✓	×
DynamicVis (2025) [27]	×	..	×	×	✓	×	×	×	×	✓	✓
FlexiMo (2025) [91]	×	..	×	×	✓	×	×	×	×	✓	✓
Google Satellite (2025)[56]	✓	×	✓	✓	✓	×	✓	✓	✓	✓	✓
RingMoE (2025) [19]	×	..	×	×	✓	✓	×	×	✓	✓	✓

References and Notes

- [1] Materials and methods are available as supplementary material.
- [2] Dynamic World V1 | Earth Engine Data Catalog. https://developers.google.com/earth-engine/datasets/catalog/GOOGLE_DYNAMICWORLD_V1.
- [3] INVEKOS Schläge Österreich 2022 - Open Government Data Austria.
- [4] Monitoring Trends in Burn Severity (ver. 12.0, April 2025) - ScienceBase-Catalog. <https://www.sciencebase.gov/catalog/item/5e541969e4b0ff554f753113>.
- [5] J. T. Abatzoglou and A. P. Williams. Impact of anthropogenic climate change on wildfire across western US forests. *Proceedings of the National Academy of Sciences*, 113(42):11770–11775, Oct. 2016.
- [6] A. A. Adegun, S. Viriri, and J.-R. Tapamo. Review of deep learning methods for remote sensing satellite images classification: experimental survey and comparative analysis. *Journal of Big Data*, 10(1):93, June 2023.
- [7] P. Akiva, M. Purri, and M. Leotta. Self-supervised material and texture representation learning for remote sensing tasks. In *2022 IEEE/CVF Conference on Computer Vision and Pattern Recognition (CVPR)*, pages 8193–8205, 2022.
- [8] M. Amani, M. Kakooei, A. Moghimi, A. Ghorbanian, B. Ranjgar, S. Mahdavi, A. Davidson, T. Fisette, P. Rollin, B. Brisco, and A. Mohammadzadeh. Application of google earth engine cloud computing platform, sentinel imagery, and neural networks for crop mapping in canada. *Remote Sensing*, 12(21), 2020.
- [9] X. An, W. He, J. Zou, G. Yang, and H. Zhang. Pretrain a remote sensing foundation model by promoting intra-instance similarity. *IEEE Transactions on Geoscience and Remote Sensing*, 62:1–15, 2024.
- [10] N. Andela, D. C. Morton, L. Giglio, Y. Chen, G. R. van der Werf, P. S. Kasibhatla, R. S. DeFries, G. J. Collatz, S. Hantson, S. Kloster, D. Bachelet, M. Forrest, G. Lasslop, F. Li, S. Mangeon, J. R. Melton, C. Yue, and J. T. Randerson. A human-driven decline in global burned area. *Science*, 356(6345):1356–1362, June 2017.
- [11] G. Astruc, N. Gonthier, C. Mallet, and L. Landrieu. Omnisat: Self-supervised modality fusion for earth observation. In *European Conference on Computer Vision*, pages 409–427. Springer, 2024.
- [12] G. Astruc, N. Gonthier, C. Mallet, and L. Landrieu. Anysat: One earth observation model for many resolutions, scales, and modalities, 2025.
- [13] C. Atzberger, M. Immitzer, K. S. Hemes, M. Kästenbauer, J. López, T. Terra, C. Rajadel-Lambistos, S. F. de Souza, K. Trabaquini, and N. Wolff. A scalable, annual aboveground biomass product for monitoring carbon impacts of ecosystem restoration projects. *Remote Sensing of Environment*, 327:114774, 2025.
- [14] K. Ayush, B. Uzkent, C. Meng, K. Tanmay, M. Burke, D. Lobell, and S. Ermon. Geography-aware self-supervised learning. In *2021 IEEE/CVF International Conference on Computer Vision (ICCV)*, pages 10161–10170, 2021.
- [15] R. Balestriero, M. Ibrahim, V. Sobal, A. Morcos, S. Shekhar, T. Goldstein, F. Bordes, A. Bardes, G. Mialon, Y. Tian, A. Schwarzschild, A. G. Wilson, J. Geiping, Q. Garrido, P. Fernandez, A. Bar, H. Pirsiavash, Y. LeCun, and M. Goldblum. A cookbook of self-supervised learning, 2023.
- [16] W. G. C. Bandara, C. M. D. Melo, and V. M. Patel. Guarding barlow twins against overfitting with mixed samples, 2023.
- [17] H. B. Barlow. Redundancy reduction revisited. *Network: Computation in Neural Systems*, 12:241 – 253, 2001.
- [18] F. Bastani, P. Wolters, R. Gupta, J. Ferdinando, and A. Kembhavi. SatlasPretrain: A Large-Scale Dataset for Remote Sensing Image Understanding . In *2023 IEEE/CVF International Conference on Computer Vision (ICCV)*, pages 16726–16736, Los Alamitos, CA, USA, Oct. 2023. IEEE Computer Society.

- [19] H. Bi, Y. Feng, B. Tong, M. Wang, H. Yu, Y. Mao, H. Chang, W. Diao, P. Wang, Y. Yu, H. Peng, Y. Zhang, K. Fu, and X. Sun. Ringmoe: Mixture-of-modality-experts multi-modal foundation models for universal remote sensing image interpretation, 2025.
- [20] K. Bi, L. Xie, H. Zhang, X. Chen, X. Gu, and Q. Tian. Accurate medium-range global weather forecasting with 3d neural networks. *Nature*, 619:533–538, 2023.
- [21] C. Bodnar, W. P. Bruinsma, A. Lucic, M. Stanley, A. Allen, J. Brandstetter, P. Garvan, M. Riechert, J. A. Weyn, H. Dong, J. K. Gupta, K. Thambiratnam, A. T. Archibald, C.-C. Wu, E. Heider, M. Welling, R. E. Turner, and P. Perdikaris. A foundation model for the earth system. *Nature*, 641:1180–1187, 2025.
- [22] N. I. Bountos, A. Ouaknine, I. Papoutsis, and D. Rolnick. Fomo: Multi-modal, multi-scale and multi-task remote sensing foundation models for forest monitoring, 2025.
- [23] J. Bourcier, G. Dashyan, K. Alahari, and J. Chanusot. Learning representations of satellite images from metadata supervision. In A. Leonardis, E. Ricci, S. Roth, O. Russakovsky, T. Sattler, and G. Varol, editors, *Computer Vision – ECCV 2024*, volume 15085 of *Lecture Notes in Computer Science*, page 4. Springer, Cham, 2025.
- [24] D. Butler. Earth observation enters next phase. *Nature*, 508(7495):160–161, 2014.
- [25] R. Cazzolla Gatti, A. Di Paola, A. Bombelli, S. Noce, and R. Valentini. Exploring the relationship between canopy height and terrestrial plant diversity. *Plant Ecology*, 218(7):899–908, July 2017.
- [26] K. Cha, J. Seo, and T. Lee. A billion-scale foundation model for remote sensing images. *IEEE Journal of Selected Topics in Applied Earth Observations and Remote Sensing*, page 1–17, 2024.
- [27] K. Chen, C. Liu, B. Chen, W. Li, Z. Zou, and Z. Shi. Dynamicvis: An efficient and general visual foundation model for remote sensing image understanding, 2025.
- [28] K. Chen, C. Liu, H. Chen, H. Zhang, W. Li, Z. Zou, and Z. Shi. Rsprompter: Learning to prompt for remote sensing instance segmentation based on visual foundation model. *IEEE Transactions on Geoscience and Remote Sensing*, 2024.
- [29] Y. Chen, D. C. Morton, N. Andela, L. Giglio, and J. T. Randerson. How much global burned area can be forecast on seasonal time scales using sea surface temperatures? *Environ. Res. Lett.*, 11(4):045001, Mar. 2016.
- [30] E. Chuvieco, F. Mouillot, G. R. van der Werf, J. San Miguel, M. Tanase, N. Koutsias, M. García, M. Yebra, M. Padilla, I. Gitas, A. Heil, T. J. Hawbaker, and L. Giglio. Historical background and current developments for mapping burned area from satellite Earth observation. *Remote Sensing of Environment*, 225:45–64, May 2019.
- [31] Clay Foundation Team. Clay foundation model: An open source ai model and interface for earth. <https://madewithclay.org>, 2023. Version 0.0.1, Apache License, code and model weights available on GitHub and Hugging Face.
- [32] Y. Cong, S. Khanna, C. Meng, P. Liu, E. Rozi, Y. He, M. Burke, D. B. Lobell, and S. Ermon. Satmae: pre-training transformers for temporal and multi-spectral satellite imagery. In *Proceedings of the 36th International Conference on Neural Information Processing Systems*, NIPS ’22, Red Hook, NY, USA, 2022. Curran Associates Inc.
- [33] D. Coomes and T. Jackson. Airborne LiDAR and RGB imagery from Sepilok Reserve and Danum Valley in Malaysia in 2020, 2022.
- [34] C. Corbane, P. Politis, P. Kempeneers, D. Simonetti, P. Soille, A. Burger, M. Pesaresi, F. Sabo, V. Syrris, and T. Kemper. A global cloud free pixel- based image composite from sentinel-2 data. *Data in Brief*, 31:105737, 2020.
- [35] I. Corley and C. Robinson. Hydro foundation model. <https://github.com/isaaccorley/hydro-foundation-model>, 2024.
- [36] R. Daroya, E. Cole, O. M. Aodha, G. V. Horn, and S. Maji. Wildsat: Learning satellite image representations from wildlife observations, 2024.
- [37] A. B. Davies and G. P. Asner. Advances in animal ecology from 3D-LiDAR ecosystem mapping. *Trends in Ecology & Evolution*, 29(12):681–691, Dec. 2014.

- [38] W. Diao, H. Yu, K. Kang, T. Ling, D. Liu, Y. Feng, H. Bi, L. Ren, X. Li, Y. Mao, and X. Sun. Ringmo-aerial: An aerial remote sensing foundation model with affine transformation contrastive learning, 2025.
- [39] P. Dias, A. Tsaris, J. Bowman, A. Potnis, J. Arndt, H. L. Yang, and D. Lunga. Oreolefm: successes and challenges toward billion-parameter foundation models for high-resolution satellite imagery. In *Proceedings of the 32nd ACM International Conference on Advances in Geographic Information Systems, SIGSPATIAL '24*, page 597–600. ACM, Oct. 2024.
- [40] Z. Dong, Y. Gu, and T. Liu. Generative convnet foundation model with sparse modeling and low-frequency reconstruction for remote sensing image interpretation. *IEEE Transactions on Geoscience and Remote Sensing*, 62:1–16, 2024.
- [41] R. Dubayah, J. B. Blair, S. Goetz, L. Fatoyinbo, M. Hansen, S. Healey, M. Hofton, G. Hurtt, J. Kellner, S. Luthcke, J. Armston, H. Tang, L. Duncanson, S. Hancock, P. Jantz, S. Marselis, P. L. Patterson, W. Qi, and C. Silva. The Global Ecosystem Dynamics Investigation: High-resolution laser ranging of the Earth’s forests and topography. *Science of Remote Sensing*, 1:100002, June 2020.
- [42] R. Dubayah, W. Qi, J. Armston, T. Fatoyinbo, K. Papathanassiou, M. Pardini, A. Stovall, C. Choi, and V. Cazcarra-Bes. Pantropical forest height and biomass from gedi and tandem-x data fusion. 2023.
- [43] C. M. Duc and H. Fukui. Satmamba: Development of foundation models for remote sensing imagery using state space models, 2025.
- [44] I. Dumeur, S. Valero, and J. Inglada. Self-supervised spatio-temporal representation learning of satellite image time series. *IEEE Journal of Selected Topics in Applied Earth Observations and Remote Sensing*, 17:4350–4367, 2024.
- [45] L. Duncanson, J. Armston, M. Disney, V. Avitabile, N. Barbier, K. Calders, S. Carter, J. Chave, M. Herold, T. Crowther, M. Falkowski, J. Kellner, N. Labriere, R. Lucas, N. MacBean, R. Mcroberts, V. Meyer, E. Næsset, J. Nickeson, and M. Williams. The importance of consistent validation of global forest aboveground biomass products. *Surveys in Geophysics*, 40, 07 2019.
- [46] European Space Agency. Sentinel-1 data. Copernicus Data Space Ecosystem, 2014–present.
- [47] European Space Agency. Sentinel-2 data. Copernicus Data Space Ecosystem, 2015–present.
- [48] European Space Agency (ESA). SNAP - ESA Sentinel Application Platform, 2024.
- [49] T. R. Feldpausch, J. Lloyd, S. L. Lewis, R. J. W. Brienen, M. Gloor, A. Monteagudo Mendoza, G. Lopez-Gonzalez, L. Banin, K. Abu Salim, K. Affum-Baffoe, M. Alexiades, S. Almeida, I. Amaral, A. Andrade, L. E. O. C. Aragão, A. Araujo Murakami, E. J. M. M. Arets, L. Arroyo, G. A. Aymard C., T. R. Baker, O. S. Bánki, N. J. Berry, N. Cardozo, J. Chave, J. A. Comiskey, E. Alvarez, A. de Oliveira, A. Di Fiore, G. Djagbletey, T. F. Domingues, T. L. Erwin, P. M. Fearnside, M. B. França, M. A. Freitas, N. Higuchi, E. H. C. Y. Iida, E. Jiménez, A. R. Kassim, T. J. Killeen, W. F. Laurance, J. C. Lovett, Y. Malhi, B. S. Marimon, B. H. Marimon-Junior, E. Lenza, A. R. Marshall, C. Mendoza, D. J. Metcalfe, E. T. A. Mitchard, D. A. Neill, B. W. Nelson, R. Nilus, E. M. Nogueira, A. Parada, K. S.-H. Peh, A. Pena Cruz, M. C. Peñuela, N. C. A. Pitman, A. Prieto, C. A. Quesada, F. Ramírez, H. Ramírez-Angulo, J. M. Reitsma, A. Rudas, G. Saiz, R. P. Salomão, M. Schwarz, N. Silva, J. E. Silva-Espejo, M. Silveira, B. Sonké, J. Stropp, H. E. Taedoung, S. Tan, H. ter Steege, J. Terborgh, M. Torello-Raventos, G. M. F. van der Heijden, R. Vásquez, E. Vilanova, V. A. Vos, L. White, S. Willcock, H. Woell, and O. L. Phillips. Tree height integrated into pantropical forest biomass estimates. *Biogeosciences*, 9(8):3381–3403, Aug. 2012.
- [50] Y. Feng, P. Wang, W. Diao, Q. He, H. Hu, H. Bi, X. Sun, and K. Fu. A self-supervised cross-modal remote sensing foundation model with multi-domain representation and cross-domain fusion. In *IGARSS 2023 - 2023 IEEE International Geoscience and Remote Sensing Symposium*, pages 2239–2242, 2023.
- [51] F. J. Fischer, T. Jackson, G. Vincent, and T. Jucker. Robust characterisation of forest structure from airborne laser scanning—A systematic assessment and sample workflow for ecologists. *Methods in Ecology and Evolution*, 15(10):1873–1888, 2024.

- [52] L. Fu, Q. Shu, Z. Yang, C. Xia, X. Zhang, Y. Zhang, Z. Li, and S. Li. Accuracy assessment of topography and forest canopy height in complex terrain conditions of Southern China using ICESat-2 and GEDI data. *Frontiers in Plant Science*, 16, Mar. 2025.
- [53] A. Fuller, K. Millard, and J. Green. Croma: Remote sensing representations with contrastive radar-optical masked autoencoders. *Advances in Neural Information Processing Systems*, 36:5506–5538, 2023.
- [54] Q. Garrido, R. Balestriero, L. Najman, and Y. Lecun. Rankme: Assessing the downstream performance of pretrained self-supervised representations by their rank. In *International conference on machine learning*, pages 10929–10974. PMLR, 2023.
- [55] B. L. Giddey, J. A. Baard, and T. Kraaij. Verification of the differenced Normalised Burn Ratio (dNBR) as an index of fire severity in Afrotropical Forest. *South African Journal of Botany*, 146:348–353, May 2022.
- [56] Google and Google DeepMind. Google satellite embedding v1. https://developers.google.com/earth-engine/datasets/catalog/GOOGLE_SATELLITE_EMBEDDING_V1_ANNUAL. This dataset is produced by Google and Google DeepMind. Licensed under CC-BY 4.0.
- [57] Google LLC. Google Earth Engine: Planetary-scale geospatial analysis. Web page, 2025. Accessed: 2025-07-22.
- [58] Google LLC. Vertex AI: A fully-managed, end-to-end ML platform. Web page, 2025. Accessed: 2025-07-22.
- [59] X. Guo, J. Lao, B. Dang, Y. Zhang, L. Yu, L. Ru, L. Zhong, Z. Huang, K. Wu, D. Hu, H. He, J. Wang, J. Chen, M. Yang, Y. Zhang, and Y. Li. Skysense: A multi-modal remote sensing foundation model towards universal interpretation for earth observation imagery. In *2024 IEEE/CVF Conference on Computer Vision and Pattern Recognition (CVPR)*, pages 27662–27673, 2024.
- [60] C. Gómez, J. C. White, and M. A. Wulder. Optical remotely sensed time series data for land cover classification: A review. *ISPRS Journal of Photogrammetry and Remote Sensing*, 116:55–72, June 2016.
- [61] B. Han, S. Zhang, X. Shi, and M. Reichstein. Bridging remote sensors with multisensor geospatial foundation models. In *2024 IEEE/CVF Conference on Computer Vision and Pattern Recognition (CVPR)*, pages 27852–27862, 2024.
- [62] C. R. Harris, K. J. Millman, S. J. van der Walt, R. Gommers, P. Bird, J. Kernfeld, et al. Array programming with numpy. *Nature*, 585:357–362, 2020.
- [63] Y. Hashida, D. J. Lewis, and K. Cummins. Prescribed fires as a climate change adaptation tool. *Journal of Environmental Economics and Management*, 130:103081, Mar. 2025.
- [64] T. J. Hawbaker, V. C. Radeloff, A. D. Syphard, Z. Zhu, and S. I. Stewart. Detection rates of the MODIS active fire product in the United States. *Remote Sensing of Environment*, 112(5):2656–2664, May 2008.
- [65] T. J. Hawbaker, M. K. Vanderhoof, Y.-J. Beal, J. D. Takacs, G. L. Schmidt, J. T. Falgout, B. Williams, N. M. Fairaux, M. K. Caldwell, J. J. Picotte, S. M. Howard, S. Stitt, and J. L. Dwyer. Mapping burned areas using dense time-series of Landsat data. *Remote Sensing of Environment*, 198:504–522, Sept. 2017.
- [66] M. Herold, S. Carter, V. Avitabile, A. Espejo, I. Jonckheere, R. Lucas, R. Mcroberts, E. Næsset, J. Nightingale, R. Petersen, J. Reiche, E. Romijn, A. Rosenqvist, D. Rozendaal, F. M. Seifert, M.-J. Sanz-Sanchez, and V. De Sy. The role and need for space-based forest biomass-related measurements in environmental management and policy. *Surveys in Geophysics*, 40, 07 2019.
- [67] D. Hong, B. Zhang, X. Li, Y. Li, C. Li, J. Yao, N. Yokoya, H. Li, P. Ghamisi, X. Jia, A. Plaza, P. Gamba, J. A. Benediktsson, and J. Chanussot. Spectralgpt: Spectral remote sensing foundation model. *IEEE Transactions on Pattern Analysis and Machine Intelligence*, 46(8):5227–5244, Aug. 2024.
- [68] H. Hu, P. Wang, H. Bi, B. Tong, Z. Wang, W. Diao, H. Chang, Y. Feng, Z. Zhang, Y. Wang, Q. Ye, K. Fu, and X. Sun. Rs-vheat: Heat conduction guided efficient remote sensing foundation model, 2025.

- [69] Z. Huang, M. Zhang, Y. Gong, Q. Liu, and Y. Wang. Generic knowledge boosted pre-training for remote sensing images, 2024.
- [70] A. V. Huynh, L. E. Gillespie, J. Lopez-Saucedo, C. Tang, R. Sikand, and M. Expósito-Alonso. Contrastive ground-level image and remote sensing pre-training improves representation learning for natural world imagery. In A. Leonardis, E. Ricci, S. Roth, O. Russakovsky, T. Sattler, and G. Varol, editors, *Computer Vision – ECCV 2024*, volume 15138 of *Lecture Notes in Computer Science*, page 10. Springer, Cham, 2025.
- [71] V. Iglesias, J. K. Balch, and W. R. Travis. U.S. fires became larger, more frequent, and more widespread in the 2000s. *Science Advances*, 8(11):eabc0020, Mar. 2022.
- [72] J. Irvin, L. Tao, J. Zhou, Y. Ma, L. Nashold, B. Liu, and A. Y. Ng. Usat: A unified self-supervised encoder for multi-sensor satellite imagery, 2023.
- [73] Jack-bo1220. Awesome remote sensing foundation models. <https://github.com/Jack-bo1220/Awesome-Remote-Sensing-Foundation-Models>, 2025. A collection of papers, datasets, benchmarks, code, and pre-trained weights for Remote Sensing Foundation Models (RSFMs).
- [74] T. D. Jackson, F. J. Fischer, G. Vincent, E. B. Gorgens, M. Keller, J. Chave, T. Jucker, and D. A. Coomes. Tall Bornean forests experience higher canopy disturbance rates than those in the eastern Amazon or Guiana shield. *Global Change Biology*, 30, 2024.
- [75] P. Jain, B. Schoen-Phelan, and R. Ross. Self-supervised learning for invariant representations from multi-spectral and sar images. *IEEE Journal of Selected Topics in Applied Earth Observations and Remote Sensing*, 15:7797–7808, 2022.
- [76] J. Jakubik, S. Roy, C. E. Phillips, P. Fraccaro, D. Godwin, B. Zadrozny, D. Szwarcman, C. Gomes, G. Nyirjesy, B. Edwards, D. Kimura, N. Simumba, L. Chu, S. K. Mukkavilli, D. Lambhate, K. Das, R. Bangalore, D. Oliveira, M. Muszynski, K. Ankur, M. Ramasubramanian, I. Gurung, S. Khallaghi, Hanxi, Li, M. Cecil, M. Ahmadi, F. Kordi, H. Alemohammad, M. Maskey, R. Ganti, K. Weldemariam, and R. Ramachandran. Foundation Models for Generalist Geospatial Artificial Intelligence, Nov. 2023.
- [77] Y. Jia, V. Marsocci, Z. Gong, X. Yang, M. Vergauwen, and A. Nascetti. Can generative geospatial diffusion models excel as discriminative geospatial foundation models?, 2025.
- [78] W. Jiang, J. Zhang, D. Wang, Q. Zhang, Z. Wang, and B. Du. Lemevit: Efficient vision transformer with learnable meta tokens for remote sensing image interpretation, 2024.
- [79] A. Joshi, B. Pradhan, S. Gite, and S. Chakraborty. Remote-Sensing Data and Deep-Learning Techniques in Crop Mapping and Yield Prediction: A Systematic Review. *Remote Sensing*, 15(8):2014, Jan. 2023. Number: 8 Publisher: Multidisciplinary Digital Publishing Institute.
- [80] S. Khanna, P. Liu, L. Zhou, C. Meng, R. Rombach, M. Burke, D. B. Lobell, and S. Ermon. Diffusionsat: A generative foundation model for satellite imagery. In *The Twelfth International Conference on Learning Representations*, 2024.
- [81] K. Klemmer, E. Rolf, C. Robinson, L. Mackey, and M. Rußwurm. Satclip: Global, general-purpose location embeddings with satellite imagery. *Proceedings of the AAAI Conference on Artificial Intelligence*, 39(4):4347–4355, Apr. 2025.
- [82] E. Kurbanov, O. Vorobev, S. Lezhnin, J. Sha, J. Wang, X. Li, J. Cole, D. Dergunov, and Y. Wang. Remote Sensing of Forest Burnt Area, Burn Severity, and Post-Fire Recovery: A Review. *Remote Sensing*, 14(19):4714, Jan. 2022.
- [83] K. Lahssini, N. Baghdadi, G. le Maire, I. Fayad, and L. Villard. Canopy height mapping in French Guiana using multi-source satellite data and environmental information in a U-Net architecture. *Frontiers in Remote Sensing*, 5, Nov. 2024.
- [84] N. Lang, W. Jetz, K. Schindler, and J. D. Wegner. A high-resolution canopy height model of the Earth. *Nature Ecology & Evolution*, 7(11):1778–1789, Nov. 2023.
- [85] N. Lang, K. Schindler, and J. D. Wegner. High carbon stock mapping at large scale with optical satellite imagery and spaceborne LIDAR, July 2021.
- [86] J. Li, Y. Liu, X. Wang, Y. Peng, C. Sun, S. Wang, Z. Sun, T. Ke, X. Jiang, T. Lu, A. Zhao, and Y. Zhong. Hyperfree: A channel-adaptive and tuning-free foundation model for hyperspectral remote sensing imagery. In *Proceedings of the IEEE/CVF Conference on Computer Vision and Pattern Recognition (CVPR)*, 2025.

- [87] W. Li, K. Chen, H. Chen, and Z. Shi. Geographical knowledge-driven representation learning for remote sensing images. *IEEE Transactions on Geoscience and Remote Sensing*, 60:1–16, 2022.
- [88] W. Li, K. Chen, and Z. Shi. Geographical supervision correction for remote sensing representation learning. *IEEE Transactions on Geoscience and Remote Sensing*, 60:1–20, 2022.
- [89] W. Li, W. Yang, T. Liu, Y. Hou, Y. Li, Z. Liu, Y. Liu, and L. Liu. Predicting gradient is better: Exploring self-supervised learning for sar atr with a joint-embedding predictive architecture. *ISPRS Journal of Photogrammetry and Remote Sensing*, 218:326–338, 2024.
- [90] X. Li, D. Hong, and J. Chanussot. S2mae: A spatial-spectral pretraining foundation model for spectral remote sensing data. In *Proceedings of the IEEE/CVF Conference on Computer Vision and Pattern Recognition*, pages 24088–24097, 2024.
- [91] X. Li, C. Li, P. Ghamisi, and D. Hong. Fleximo: A flexible remote sensing foundation model, 2025.
- [92] X. Li, C. Li, G. Vivone, and D. Hong. Seamo: A season-aware multimodal foundation model for remote sensing, 2025.
- [93] Z. Li, B. Hou, S. Ma, Z. Wu, X. Guo, B. Ren, and L. Jiao. Masked angle-aware autoencoder for remote sensing images, 2024.
- [94] Z. Li, B. Hou, S. Ma, Z. Wu, X. Guo, B. Ren, and L. Jiao. Masked angle-aware autoencoder for remote sensing images. In *European Conference on Computer Vision*, pages 260–278. Springer, 2025.
- [95] M. C. Lisaius, A. Blake, S. Keshav, and C. Atzberger. Using barlow twins to create representations from cloud-corrupted remote sensing time series. *IEEE Journal of Selected Topics in Applied Earth Observations and Remote Sensing*, 17:13162–13168, 2024.
- [96] A. Liu, Y. Chen, and X. Cheng. Improving Tropical Forest Canopy Height Mapping by Fusion of Sentinel-1/2 and Bias-Corrected ICESat-2–GEDI Data. *Remote Sensing*, 17(12):1968, Jan. 2025.
- [97] X. Liu, F. Zhang, Z. Hou, L. Mian, Z. Wang, J. Zhang, and J. Tang. Self-supervised learning: Generative or contrastive. *IEEE Transactions on Knowledge and Data Engineering*, page 1–1, 2021.
- [98] K. Lu, R. Zhang, X. Huang, Y. Xie, X. Ning, H. Zhang, M. Yuan, P. Zhang, T. Wang, and T. Liao. Pattern integration and enhancement vision transformer for self-supervised learning in remote sensing. *IEEE Transactions on Geoscience and Remote Sensing*, 2025.
- [99] G. Mai, N. Lao, Y. He, J. Song, and S. Ermon. Csp: self-supervised contrastive spatial pre-training for geospatial-visual representations. In *Proceedings of the 40th International Conference on Machine Learning, ICML’23*. JMLR.org, 2023.
- [100] U. Mall, B. Hariharan, and K. Bala. Change-aware sampling and contrastive learning for satellite images. In *Proceedings of the IEEE/CVF Conference on Computer Vision and Pattern Recognition (CVPR)*, pages 5261–5270, June 2023.
- [101] V. Marsocci, Y. Jia, G. L. Bellier, D. Kerekes, L. Zeng, S. Hafner, S. Gerard, E. Brune, R. Yadav, A. Shibli, H. Fang, Y. Ban, M. Vergauwen, N. Audebert, and A. Nascetti. Pangaea: A global and inclusive benchmark for geospatial foundation models, 2025.
- [102] O. Mañas, A. Lacoste, X. Giró-i Nieto, D. Vazquez, and P. Rodríguez. Seasonal contrast: Un-supervised pre-training from uncurated remote sensing data. In *2021 IEEE/CVF International Conference on Computer Vision (ICCV)*, pages 9394–9403, 2021.
- [103] L. McInnes, J. Healy, and J. Melville. Umap: Uniform manifold approximation and projection for dimension reduction. *arXiv preprint arXiv:1802.03426*, 2018.
- [104] M. Mendieta, B. Han, X. Shi, Y. Zhu, and C. Chen. Towards geospatial foundation models via continual pretraining. In *2023 IEEE/CVF International Conference on Computer Vision (ICCV)*, pages 16760–16770, 2023.
- [105] M. Migliavacca, T. Musavi, M. D. Mahecha, J. A. Nelson, J. Knauer, D. D. Baldocchi, O. Perez-Priego, R. Christiansen, J. Peters, K. Anderson, M. Bahn, T. A. Black, P. D. Blanken, D. Bonal, N. Buchmann, S. Caldararu, A. Carrara, N. Carvalhais, A. Cescatti, J. Chen, J. Cleverly, E. Cremonese, A. R. Desai, T. S. El-Madany, M. M. Farella, M. Fernández-Martínez,

- G. Filippa, M. Forkel, M. Galvagno, U. Gomasasca, C. M. Gough, M. Göckede, A. Ibrom, H. Ikawa, I. A. Janssens, M. Jung, J. Kattge, T. F. Keenan, A. Knohl, H. Kobayashi, G. Kraemer, B. E. Law, M. J. Liddell, X. Ma, I. Mammarella, D. Martini, C. Macfarlane, G. Matteucci, L. Montagnani, D. E. Pabon-Moreno, C. Panigada, D. Papale, E. Pendall, J. Penuelas, R. P. Phillips, P. B. Reich, M. Rossini, E. Rotenberg, R. L. Scott, C. Stahl, U. Weber, G. Wohlfahrt, S. Wolf, I. J. Wright, D. Yakir, S. Zaehle, and M. Reichstein. The three major axes of terrestrial ecosystem function. *Nature*, 598(7881):468–472, Oct. 2021.
- [106] A. L. Mitchell, A. Rosenqvist, and B. Mora. Current remote sensing approaches to monitoring forest degradation in support of countries measurement, reporting and verification (MRV) systems for REDD+. *Carbon Balance and Management*, 12(1):9, Apr. 2017.
- [107] V. Moudrý, L. Gábor, S. Marselis, P. Pracná, V. Barták, J. Prošek, B. Navrátilová, J. Novotný, M. Potůčková, K. Gdulová, P. Crespo-Peremarch, J. Komárek, M. Malavasi, D. Rocchini, L. A. Ruiz, J. Torralba, M. Torresani, R. Cazzolla Gatti, and J. Wild. Comparison of three global canopy height maps and their applicability to biodiversity modeling: Accuracy issues revealed. *Ecosphere*, 15(10):e70026, 2024.
- [108] V. Moudrý, R. Remelgado, M. Forkel, M. Torresani, G. V. Laurin, E. Sarovcova, V. E. G. Millan, F. J. Fischer, T. Jucker, M. Gally, P. Kacic, C. R. Hakkenberg, Ž. Kokalj, K. Stereńczak, Y. Erfanifard, D. Rocchini, J. Prošek, S. Roilo, K. Gdulova, A. F. Cord, M. Perrone, J. A. Molina-Valero, P. Surovy, Z. Melichová, M. Malavasi, R. Urban, M. Štroner, D. Seidel, S. Szabó, L. Bertalan, A. Etner, R. C. Gatti, and V. Barták. Harmonised airborne laser scanning products can address the limitations of large-scale spaceborne vegetation mapping. Dec. 2024.
- [109] D. Muhtar, X. Zhang, P. Xiao, Z. Li, and F. Gu. Cmid: A unified self-supervised learning framework for remote sensing image understanding. *IEEE Transactions on Geoscience and Remote Sensing*, 61:1–17, 2023.
- [110] P. K. Mutuo, G. Cadisch, A. Albrecht, C. Palm, and L. Verchot. Potential of agroforestry for carbon sequestration and mitigation of greenhouse gas emissions from soils in the tropics. *Nutrient cycling in Agroecosystems*, 71(1):43–54, 2005.
- [111] A. Nascetti, R. Yadav, K. Brodt, Q. Qu, H. Fan, Y. Shendryk, I. Shah, and C. Chung. Biomasters: A benchmark dataset for forest biomass estimation using multi-modal satellite time-series. In *Thirty-seventh Conference on Neural Information Processing Systems Datasets and Benchmarks Track*, 2023.
- [112] V. Nedungadi, A. Kariryaa, S. Oehmcke, S. J. Belongie, C. Igel, and N. Lang. Mmearth: Exploring multi-modal pretext tasks for geospatial representation learning. In A. Leonardis, E. Ricci, S. Roth, O. Russakovsky, T. Sattler, and G. Varol, editors, *Computer Vision - ECCV 2024 - 18th European Conference, Milan, Italy, September 29-October 4, 2024, Proceedings, Part LXIV*, volume 15122 of *Lecture Notes in Computer Science*, pages 164–182. Springer, 2024.
- [113] M. Noman, M. Naseer, H. Cholakkal, R. M. Anwar, S. Khan, and F. S. Khan. Rethinking Transformers Pre-training for Multi-Spectral Satellite Imagery . In *2024 IEEE/CVF Conference on Computer Vision and Pattern Recognition (CVPR)*, pages 27811–27819, Los Alamitos, CA, USA, June 2024. IEEE Computer Society.
- [114] A. O. Ok, A. , Ozlem, , and O. Gungor. Evaluation of random forest method for agricultural crop classification. *European Journal of Remote Sensing*, 45(1):421–432, Jan. 2012. Publisher: Taylor & Francis _eprint: <https://doi.org/10.5721/EuJRS20124535>.
- [115] L. Pang, D. Tang, S. Xu, D. Meng, and X. Cao. Hsigene: A foundation model for hyperspectral image generation, 2024.
- [116] J. Pauls, M. Zimmer, B. Turan, S. Saatchi, P. Ciais, S. Pokutta, and F. Gieseke. Capturing Temporal Dynamics in Large-Scale Canopy Tree Height Estimation. <https://arxiv.org/abs/2501.19328v1>, Jan. 2025.
- [117] O. Pechony, D. T. Shindell, and F. S. Chapin. Driving forces of global wildfires over the past millennium and the forthcoming century. *Proceedings of the National Academy of Sciences of the United States of America*, 107(45):19167–19170, 2010.

- [118] N. Pettorelli, H. Schulte to Bühne, A. Tulloch, G. Dubois, C. Macinnis-Ng, A. M. Queirós, D. A. Keith, M. Wegmann, F. Schrod, M. Stellmes, et al. Satellite remote sensing of ecosystem functions: opportunities, challenges and way forward. *Remote Sensing in Ecology and Conservation*, 4(2):71–93, 2018.
- [119] J. J. Picotte, K. Bhattarai, D. Howard, J. Lecker, J. Epting, B. Quayle, N. Benson, and K. Nelson. Changes to the Monitoring Trends in Burn Severity program mapping production procedures and data products. *Fire Ecology*, 16(1):16, June 2020.
- [120] C. Piloniot, K. J. Anderson-Teixeira, S. J. Davies, D. Allen, N. A. Bourg, D. F. R. P. Burslem, D. Cárdenas, C.-H. Chang-Yang, G. Chuyong, S. Cordell, H. S. Dattaraja, Á. Duque, S. Ediriweera, C. Ewango, Z. Ezedin, J. Filip, C. P. Giardina, R. Howe, C.-F. Hsieh, S. P. Hubbell, F. M. Inman-Narahari, A. Itoh, D. Janík, D. Kenfack, K. Král, J. A. Lutz, J.-R. Makana, S. M. McMahon, W. McShea, X. Mi, M. Bt. Mohamad, V. Novotný, M. J. O’Brien, R. Ostertag, G. Parker, R. Pérez, H. Ren, G. Reynolds, M. D. Md Sabri, L. Sack, A. Shringi, S.-H. Su, R. Sukumar, I.-F. Sun, H. S. Suresh, D. W. Thomas, J. Thompson, M. Uriarte, J. Vandermeer, Y. Wang, I. M. Ware, G. D. Weiblen, T. J. S. Whitfield, A. Wolf, T. L. Yao, M. Yu, Z. Yuan, J. K. Zimmerman, D. Zuleta, and H. C. Muller-Landau. Distribution of biomass dynamics in relation to tree size in forests across the world. *New Phytologist*, 234(5):1664–1677, 2022.
- [121] P. Potapov, X. Li, A. Hernandez-Serna, A. Tyukavina, M. C. Hansen, A. Kommareddy, A. Pickens, S. Turubanova, H. Tang, C. E. Silva, J. Armston, R. Dubayah, J. B. Blair, and M. Hofton. Mapping global forest canopy height through integration of GEDI and Landsat data. *Remote Sensing of Environment*, 253:112165, Feb. 2021.
- [122] J. Prexl and M. Schmitt. Multi-modal multi-objective contrastive learning for sentinel-1/2 imagery. In *Proceedings of the IEEE/CVF Conference on Computer Vision and Pattern Recognition (CVPR) Workshops*, pages 2136–2144, June 2023.
- [123] J. Prexl and M. Schmitt. Senpa-mae: Sensor parameter aware masked autoencoder for multi-satellite self-supervised pretraining, 2024.
- [124] Python Packaging Authority. Pypi - the python package index. <https://pypi.org/>. Accessed: 2025-07-22.
- [125] P. Ravirathinam, A. Khandelwal, R. Ghosh, and V. Kumar. A causally informed pretraining approach for multimodal foundation models: Applications in remote sensing. *arXiv preprint arXiv:2407.19660*, 2024.
- [126] C. J. Reed, R. Gupta, S. Li, S. Brockman, C. Funk, B. Clipp, K. Keutzer, S. Candido, M. Uytendaele, and T. Darrell. Scale-MAE: A Scale-Aware Masked Autoencoder for Multiscale Geospatial Representation Learning. In *2023 IEEE/CVF International Conference on Computer Vision (ICCV)*, pages 4065–4076, Los Alamitos, CA, USA, Oct. 2023. IEEE Computer Society.
- [127] E. Rolf, L. Gordon, M. Tambe, and A. Davies. Contrasting local and global modeling with machine learning and satellite data: A case study estimating tree canopy height in African savannas, Nov. 2024.
- [128] O. Ronneberger, P. Fischer, and T. Brox. U-Net: Convolutional Networks for Biomedical Image Segmentation, May 2015.
- [129] E. Roteta, A. Bastarrika, M. Padilla, T. Storm, and E. Chuvieco. Development of a Sentinel-2 burned area algorithm: Generation of a small fire database for sub-Saharan Africa. *Remote Sensing of Environment*, 222:1–17, Mar. 2019.
- [130] D. P. Roy, M. A. Wulder, T. R. Loveland, C. E. Woodcock, R. G. Allen, M. C. Anderson, D. Helder, J. R. Irons, D. M. Johnson, R. Kennedy, et al. Landsat-8: Science and product vision for terrestrial global change research. *Remote Sensing of Environment*, 145:154–172, 2014.
- [131] Y. Sadeghi, B. St-Onge, B. Leblon, and M. Simard. Canopy height model (chm) derived from a tandem-x insar dsm and an airborne lidar dtm in boreal forest. *IEEE Journal of Selected Topics in Applied Earth Observations and Remote Sensing*, 9(1):381–397, 2016.
- [132] M. Santoro and O. Cartus. Esa biomass climate change initiative (biomass_cci): Global datasets of forest above-ground biomass for the years 2010, 2015, 2016, 2017, 2018, 2019, 2020 and 2021, v5.01, 2024.

- [133] L. Scheibenreif, J. Hanna, M. Mommert, and D. Borth. Self-supervised vision transformers for land-cover segmentation and classification. In *Proceedings of the IEEE/CVF Conference on Computer Vision and Pattern Recognition (CVPR) Workshops*, pages 1422–1431, June 2022.
- [134] J. Schmude, S. Roy, W. Trojak, J. Jakubik, D. S. Civitarese, S. Singh, J. Kuehnert, K. Ankur, A. Gupta, C. E. Phillips, R. Kienzler, D. Szwarcman, V. Gaur, R. Shinde, R. Lal, A. D. Silva, J. L. G. Diaz, A. Jones, S. Pfreundschuh, A. Lin, A. Sheshadri, U. Nair, V. Anantharaj, H. Hamann, C. Watson, M. Maskey, T. J. Lee, J. B. Moreno, and R. Ramachandran. Prithvi wxc: Foundation model for weather and climate, 2024.
- [135] A. Shenkin, C. J. Chandler, D. S. Boyd, T. Jackson, M. Disney, N. Majalap, R. Nilus, G. Foody, J. bin Jami, G. Reynolds, P. Wilkes, M. E. J. Cutler, G. M. F. van der Heijden, D. F. R. P. Burslem, D. A. Coomes, L. P. Bentley, and Y. Malhi. The World’s Tallest Tropical Tree in Three Dimensions. *Front. For. Glob. Change*, 2, June 2019.
- [136] A. K. Skidmore, N. C. Coops, E. Neinavaz, A. Ali, M. E. Schaepman, M. Paganini, W. D. Kissling, P. Vihervaara, R. Darvishzadeh, H. Feilhauer, M. Fernandez, N. Fernández, N. Gorelick, I. Geijzendorffer, U. Heiden, M. Heurich, D. Hobern, S. Holzwarth, F. E. Muller-Karger, R. Van De Kerchove, A. Lausch, P. J. Leitão, M. C. Lock, C. A. Múcher, B. O’Connor, D. Rocchini, C. Roesli, W. Turner, J. K. Vis, T. Wang, M. Wegmann, and V. Wingate. Priority list of biodiversity metrics to observe from space. *Nature Ecology & Evolution*, 5(7):896–906, July 2021.
- [137] M. J. Smith, L. Fleming, and J. E. Geach. Earthpt: a time series foundation model for earth observation, 2024.
- [138] C. S. Spradlin, J. A. Caraballo-Vega, J. Li, M. L. Carroll, J. Gong, and P. M. Montesano. Satvision-toa: A geospatial foundation model for coarse-resolution all-sky remote sensing imagery, 2024.
- [139] V. Stojnic and V. Risojevic. Self-supervised learning of remote sensing scene representations using contrastive multiview coding. In *Proceedings of the IEEE/CVF Conference on Computer Vision and Pattern Recognition (CVPR) Workshops*, pages 1182–1191, June 2021.
- [140] X. Sun, P. Wang, W. Lu, Z. Zhu, X. Lu, Q. He, J. Li, X. Rong, Z. Yang, H. Chang, Q. He, G. Yang, R. Wang, J. Lu, and K. Fu. Ringmo: A remote sensing foundation model with masked image modeling. *IEEE Transactions on Geoscience and Remote Sensing*, 61:1–22, 2023.
- [141] D. Szwarcman, S. Roy, P. Fraccaro, P. E. Gislason, B. Blumenstiel, R. Ghosal, P. H. de Oliveira, J. L. de Sousa Almeida, R. Sedona, Y. Kang, S. Chakraborty, S. Wang, C. Gomes, A. Kumar, M. Truong, D. Godwin, H. Lee, C.-Y. Hsu, A. A. Asanjan, B. Mujeci, D. Shidham, T. Keenan, P. Arevalo, W. Li, H. Alemohammad, P. Olofsson, C. Hain, R. Kennedy, B. Zadrozny, D. Bell, G. Cavallaro, C. Watson, M. Maskey, R. Ramachandran, and J. B. Moreno. Prithvi-eo-2.0: A versatile multi-temporal foundation model for earth observation applications, 2025.
- [142] J. Tan, C. Zhang, B. Dang, and Y. Li. Towards privacy-preserved pre-training of remote sensing foundation models with federated mutual-guidance learning, 2025.
- [143] M. A. Tanase, M. A. Belenguer-Plomer, E. Roteta, A. Bastarrika, J. Wheeler, Á. Fernández-Carrillo, K. Tansey, W. Wiedemann, P. Navratil, S. Lohberger, F. Siegert, and E. Chuvieco. Burned Area Detection and Mapping: Intercomparison of Sentinel-1 and Sentinel-2 Based Algorithms over Tropical Africa. *Remote Sensing*, 12(2):334, Jan. 2020.
- [144] M. Tang, A. Cozma, K. Georgiou, and H. Qi. Cross-scale mae: a tale of multi-scale exploitation in remote sensing. In *Proceedings of the 37th International Conference on Neural Information Processing Systems*, NIPS ’23, Red Hook, NY, USA, 2023. Curran Associates Inc.
- [145] C. Tao, J. Qi, G. Zhang, Q. Zhu, W. Lu, and H. Li. Tov: The original vision model for optical remote sensing image understanding via self-supervised learning. *IEEE Journal of Selected Topics in Applied Earth Observations and Remote Sensing*, 16:4916–4930, 2023.
- [146] TerraClass. TerraClass: Mapeamento de uso e ocupação da terra. Accessed: July 24, 2025.
- [147] J. Tian, J. Lei, J. Zhang, W. Xie, and Y. Li. Swimdiff: Scene-wide matching contrastive learning with diffusion constraint for remote sensing image, 2024.

- [148] J. Tolan, H.-I. Yang, B. Nosarzewski, G. Couairon, H. V. Vo, J. Brandt, J. Spore, S. Majumdar, D. Haziza, J. Vamaraju, T. Moutakanni, P. Bojanowski, T. Johns, B. White, T. Tiecek, and C. Couprie. Very high resolution canopy height maps from RGB imagery using self-supervised vision transformer and convolutional decoder trained on aerial lidar. *Remote Sensing of Environment*, 300:113888, Jan. 2024.
- [149] G. Tseng, R. Cartuyvels, I. Zvonkov, M. Purohit, D. Rolnick, and H. Kerner. Lightweight, Pre-trained Transformers for Remote Sensing Timeseries, Feb. 2024. arXiv:2304.14065 [cs].
- [150] G. Tseng, A. Fuller, M. Reil, H. Herzog, P. Beukema, F. Bastani, J. R. Green, E. Shelhamer, H. Kerner, and D. Rolnick. Galileo: Learning global & local features of many remote sensing modalities, 2025.
- [151] L. Uieda, S. Soler, R. Rampin, H. van Kemenade, M. Turk, D. Shapero, A. Banihirwe, and J. Leeman. Pooch: A friend to fetch your data files. *Journal of Open Source Software*, 5(45):1943, Jan. 2020.
- [152] University of Cambridge Centre for Earth Observation. Ucam-eo project. <https://github.com/ucam-eo>. Accessed: 2025-07-22.
- [153] A. Vaswani, N. Shazeer, N. Parmar, J. Uszkoreit, L. Jones, A. N. Gomez, L. Kaiser, and I. Polosukhin. Attention is all you need. In *Proceedings of the 31st International Conference on Neural Information Processing Systems, NIPS'17*, page 6000–6010, Red Hook, NY, USA, 2017. Curran Associates Inc.
- [154] A. Verhegghen, H. Eva, G. Ceccherini, F. Achard, V. Gond, S. Gourlet-Fleury, and P. O. Cerutti. The Potential of Sentinel Satellites for Burnt Area Mapping and Monitoring in the Congo Basin Forests. *Remote Sensing*, 8(12):986, Dec. 2016.
- [155] Verra. Vm0047 afforestation, reforestation, and revegetation, v1.1. <https://verra.org/methodologies/vm0047-afforestation-reforestation-and-revegetation-v1-1/>, 2025. Verra Verified Carbon Standard (VCS) Program methodology.
- [156] F. H. Wagner, R. Dalagnol, G. Carter, M. C. M. Hirye, S. Gill, L. B. S. Takougoum, S. Favrichon, M. Keller, J. P. H. B. Ometto, L. Alves, C. Creze, S. P. George-Chacon, S. Li, Z. Liu, A. Mullissa, Y. Yang, E. G. Santos, S. R. Worden, M. Brandt, P. Ciais, S. C. Hagen, and S. Saatchi. High resolution tree height mapping of the amazon forest using planet nicfi images and lidar-informed u-net model. *arXiv preprint arXiv:2501.10600*, 2025.
- [157] L. Waldmann, A. Shah, Y. Wang, N. Lehmann, A. J. Stewart, Z. Xiong, X. X. Zhu, S. Bauer, and J. Chuang. Panopticon: Advancing any-sensor foundation models for earth observation, 2025.
- [158] C. Wang, C. Song, T. A. Schroeder, C. E. Woodcock, T. M. Pavelsky, Q. Han, and F. Yao. Interpretable Multi-Sensor Fusion of Optical and SAR Data for GEDI-Based Canopy Height Mapping in Southeastern North Carolina. *Remote Sensing*, 17(9):1536, Jan. 2025.
- [159] D. Wang, M. Hu, Y. Jin, Y. Miao, J. Yang, Y. Xu, X. Qin, J. Ma, L. Sun, C. Li, C. Fu, H. Chen, C. Han, N. Yokoya, J. Zhang, M. Xu, L. Liu, L. Zhang, C. Wu, B. Du, D. Tao, and L. Zhang. Hypersigma: Hyperspectral intelligence comprehension foundation model, 2025.
- [160] D. Wang, J. Zhang, B. Du, G.-S. Xia, and D. Tao. An empirical study of remote sensing pretraining. *IEEE Transactions on Geoscience and Remote Sensing*, 61:1–20, 2023.
- [161] D. Wang, J. Zhang, B. Du, M. Xu, L. Liu, D. Tao, and L. Zhang. Samrs: Scaling-up remote sensing segmentation dataset with segment anything model. In *Advances in Neural Information Processing Systems*, volume 36, pages 8815–8827, 2023.
- [162] D. Wang, J. Zhang, M. Xu, L. Liu, D. Wang, E. Gao, C. Han, H. Guo, B. Du, D. Tao, and L. Zhang. Mtp: Advancing remote sensing foundation model via multi-task pretraining, 2024.
- [163] D. Wang, Q. Zhang, Y. Xu, J. Zhang, B. Du, D. Tao, and L. Zhang. Advancing plain vision transformer toward remote sensing foundation model. *IEEE Transactions on Geoscience and Remote Sensing*, 61:1–15, 2023.
- [164] F. Wang, H. Wang, D. Wang, Z. Guo, Z. Zhong, L. Lan, W. Yang, and J. Zhang. Harnessing massive satellite imagery with efficient masked image modeling, 2025.
- [165] F. Wang, H. Wang, Y. Wang, D. Wang, M. Chen, H. Zhao, Y. Sun, S. Wang, L. Lan, W. Yang, and J. Zhang. Roma: Scaling up mamba-based foundation models for remote sensing, 2025.

- [166] Y. Wang, C. M. Albrecht, N. A. A. Braham, C. Liu, Z. Xiong, and X. X. Zhu. Decoupling common and unique representations for multimodal self-supervised learning, 2024.
- [167] Y. Wang, C. M. Albrecht, and X. X. Zhu. Self-supervised vision transformers for joint sar-optical representation learning, 2022.
- [168] Y. Wang, C. M. Albrecht, and X. X. Zhu. Multilabel-guided soft contrastive learning for efficient earth observation pretraining. *IEEE Transactions on Geoscience and Remote Sensing*, 62:1–16, 2024.
- [169] Y. Wang, N. A. A. Braham, Z. Xiong, C. Liu, C. M. Albrecht, and X. X. Zhu. Ssl4eos12: A large-scale multi-modal, multi-temporal dataset for self-supervised learning in earth observation. *ArXiv*, abs/2211.07044, 2022.
- [170] Y. Wang, H. H. Hernández, C. M. Albrecht, and X. X. Zhu. Feature guided masked autoencoder for self-supervised learning in remote sensing, 2023.
- [171] Y. Wang, Z. Xiong, C. Liu, A. J. Stewart, T. Dujardin, N. I. Bountos, A. Zavras, F. Gerken, I. Papoutsis, L. Leal-Taixé, and X. X. Zhu. Towards a unified copernicus foundation model for earth vision, 2025.
- [172] Y. Wang, T. Zhang, L. Zhao, L. Hu, Z. Wang, Z. Niu, P. Cheng, K. Chen, X. Zeng, Z. Wang, H. Wang, and X. Sun. Ringmo-lite: A remote sensing multi-task lightweight network with cnn-transformer hybrid framework, 2023.
- [173] Z. Wang, P. Cheng, P. Tian, Y. Wang, M. Chen, S. Duan, Z. Wang, X. Li, and X. Sun. Rs-dfm: A remote sensing distributed foundation model for diverse downstream tasks, 2024.
- [174] X. Wanyan, S. Seneviratne, S. Shen, and M. Kirley. Extending global-local view alignment for self-supervised learning with remote sensing imagery, 2024.
- [175] M. Weiss, F. Jacob, and G. Duveiller. Remote sensing for agricultural applications: A meta-review. *Remote Sensing of Environment*, 236:111402, Jan. 2020.
- [176] D. S. Willett, J. Brannock, J. Dissen, P. Keown, K. Szura, O. B. Brown, and A. Simonson. Noaa open data dissemination: Petabyte-scale earth system data in the cloud. *Science Advances*, 9(38):eadh0032, 2023.
- [177] A. Xiao, W. Xuan, H. Qi, Y. Xing, R. Ren, X. Zhang, L. Shao, and S. Lu. Cat-sam: Conditional tuning for few-shot adaptation of segment anything model. *arXiv preprint arXiv:2402.03631*, 2024.
- [178] A. Xiao, W. Xuan, J. Wang, J. Huang, D. Tao, S. Lu, and N. Yokoya. Foundation models for remote sensing and earth observation: A survey, 2025.
- [179] T. Xiao, Y. Liu, B. Zhou, Y. Jiang, and J. Sun. Unified perceptual parsing for scene understanding. In *Proceedings of the European conference on computer vision (ECCV)*, pages 418–434, 2018.
- [180] Z. Xiong, Y. Wang, F. Zhang, A. J. Stewart, J. Hanna, D. Borth, I. Papoutsis, B. L. Saux, G. Camps-Valls, and X. X. Zhu. Neural plasticity-inspired multimodal foundation model for earth observation, 2024.
- [181] Z. Xiong, Y. Wang, F. Zhang, and X. X. Zhu. One for all: Toward unified foundation models for earth vision, 2024.
- [182] H. Xu, Y. Man, M. Yang, J. Wu, Q. Zhang, and J. Wang. Analytical insight of earth: A cloud-platform of intelligent computing for geospatial big data, 2023.
- [183] Y. Yan, S. Hong, A. Chen, J. Peñuelas, C. D. Allen, W. M. Hammond, S. M. Munson, R. B. Myneni, and S. Piao. Satellite-based evidence of recent decline in global forest recovery rate from tree mortality events. *Nature Plants*, pages 1–12, 2025.
- [184] Z. Yan, J. Li, X. Li, R. Zhou, W. Zhang, Y. Feng, W. Diao, K. Fu, and X. Sun. Ringmo-sam: A foundation model for segment anything in multimodal remote-sensing images. *IEEE Transactions on Geoscience and Remote Sensing*, 61:1–16, 2023.
- [185] F. Yao, W. Lu, H. Yang, L. Xu, C. Liu, L. Hu, H. Yu, N. Liu, C. Deng, D. Tang, C. Chen, J. Yu, X. Sun, and K. Fu. Ringmo-sense: Remote sensing foundation model for spatiotemporal prediction via spatiotemporal evolution disentangling. *IEEE Transactions on Geoscience and Remote Sensing*, 61:1–21, 2023.

- [186] J. Zang, F. Qiu, and Y. Zhang. A global dataset of forest regrowth following wildfires. *Sci Data*, 11(1):1052, Sept. 2024.
- [187] J. Zbontar, L. Jing, I. Misra, Y. LeCun, and S. Deny. Barlow twins: Self-supervised learning via redundancy reduction. *ArXiv*, abs/2103.03230, 2021.
- [188] L. Zhang, Y. Zhao, R. Dong, J. Zhang, S. Yuan, S. Cao, M. Chen, J. Zheng, W. Li, W. Liu, W. Zhang, L. Feng, and H. Fu. A²-mae: A spatial-temporal-spectral unified remote sensing pre-training method based on anchor-aware masked autoencoder, 2024.
- [189] M. Zhang, Q. Liu, and Y. Wang. Ctxmim: Context-enhanced masked image modeling for remote sensing image understanding, 2024.
- [190] T. Zhang, P. Gao, H. Dong, Y. Zhuang, G. Wang, W. Zhang, and H. Chen. Consecutive pre-training: A knowledge transfer learning strategy with relevant unlabeled data for remote sensing domain. *Remote Sensing*, 14(22), 2022.
- [191] X. Zhang, Y. Liu, Y. Lin, Q. Liao, and Y. Li. Uv-sam: adapting segment anything model for urban village identification. In *Proceedings of the Thirty-Eighth AAAI Conference on Artificial Intelligence and Thirty-Sixth Conference on Innovative Applications of Artificial Intelligence and Fourteenth Symposium on Educational Advances in Artificial Intelligence*, AAAI'24/IAAI'24/EAAI'24. AAAI Press, 2024.
- [192] Z. Zheng, S. Ermon, D. Kim, L. Zhang, and Y. Zhong. Changen2: Multi-temporal remote sensing generative change foundation model. *IEEE Transactions on Pattern Analysis and Machine Intelligence*, 47(2):725–741, 2025.
- [193] Z. Zhu. Change detection using landsat time series: A review of frequencies, preprocessing, algorithms, and applications. *ISPRS Journal of Photogrammetry and Remote Sensing*, 130:370–384, 2017.